Non-Fermi liquid behaviour below the Néel temperature in the frustrated heavy Fermion magnet UAu2

Non-Fermi liquid behaviour below the Néel temperature in the frustrated heavy Fermion magnet UAu_2

Christopher D. O'Neill,[1] Julian L. Schmehr,[1] Harry D.J. Keen,[1] Luke Pritchard Cairns,[1] Dmitry A. Sokolov,[1] Andreas Hermann,[1] Didier Wermeille,[2] Pascal Manuel,[3] Frank Krüger,[3,4] and Andrew D. Huxley[1]

[1] *Centre for Science at Extreme Conditions and SUPA, School of Physics and Astronomy, University of Edinburgh, Edinburgh EH9 3JZ, United Kingdom*
[2] *XMAS, ESRF, BP220, F-38043 Grenoble, France*
[3] *ISIS Pulsed Neutron and Muon Source, STFC Rutherford Appleton Laboratory, Harwell Campus, Didcot, Oxon, OX11 0QX, United Kingdom*
[4] *London Centre for Nanotechnology, University College London, Gordon St., London, WC1H 0AH, United Kingdom*

The term Fermi liquid is almost synonymous with the metallic state. The association is known to break down at quantum critical points (QCPs) but these require precise values of tuning parameters, such as pressure and applied magnetic field, to exactly suppress a continuous phase transition temperature to the absolute zero. Three dimensional non-Fermi liquid states, apart from superconductivity, that are unshackled from a QCP are much rarer and are not currently well understood. Here, we report that the triangular lattice system UAu_2 forms such a state with a non-Fermi liquid low-temperature heat capacity $C/T \sim \log(1/T)$ and electrical resistivity $\rho(T) - \rho(0) \propto T^{1.35}$ far below its Néel temperature. The magnetic order itself has a novel structure and is accompanied by weak charge modulation that is not simply due to magnetostriction. The charge modulation continues to grow in amplitude with decreasing temperature, suggesting that charge degrees of freedom play an important role in the non-Fermi liquid behaviour. In contrast with QCPs, the heat capacity and resistivity we find are unusually resilient in magnetic field. Our results suggest that a combination of magnetic frustration and Kondo physics may result in the emergence of this novel state.

The understanding of metals and superconductors rests on the paradigm that their low-energy excitations are governed by quasiparticle excitations around a stable Fermi surface. This paradigm breaks down at quantum critical points (QCPs) in a metal [1, 2], where the emergent spatial and temporal scale invariance results in spectral functions that no longer exhibit quasiparticle poles. As the temperature is increased a region opens up about a QCP in which various quantities, such as the heat capacity and electrical resistivity, change with temperature in different ways from a Fermi liquid. A prominent example of such a non-Fermi liquid (NFL) is the "strange metal" in the copper-oxide superconductors [3], which has a T-linear resistivity instead of a leading T^2 dependence characteristic of a Fermi liquid. A QCP is in this case hidden under a superconducting dome [4]. Very recently, angle resolved photoemission spectroscopy in the high-T_c cuprate family Bi2212 have challenged this picture. They revealed an abrupt recovery of quasiparticles above a temperature independent doping level [5] coinciding with the discontinuous vanishing of the pseudogap. This suggests that the strange metal might not emerge from a QCP, but could instead be a distinct NFL state of matter and begs the question as to whether such states occur more widely.

Itinerant magnets and heavy Fermions exhibit QCPs and NFLs that are easier to study than the copper-oxides owing to lower characteristic temperatures and the ease with which they can be tuned with pressure and magnetic field [6]. However, very few NFL states (not counting superconductivity) have been found that do not emanate from a QCP [1, 7]. One rare example occurs in the high-pressure partially ordered phase of the helimagnet MnSi. It is stable over a wide pressure range and has a $T^{3/2}$ electrical resistivity power law below ~ 6 K down to the mK range [8, 9]. The presence of a large topological Hall signal suggests that a partially ordered magnetic structure with non-trivial topology may underlie the NFL [10, 11].

β-$YbAlB_4$ is magnetically unordered and an example where NFL behaviour is observed without tuning in zero field. This NFL may be the result of a very unusual QCP at exactly zero field or instead represent a unique quantum critical phase that is driven into a Fermi liquid state by an infinitesimal magnetic field [12]. However, resistivity measurements have indicated that the NFL may still be attached to a QCP that can be reached with pressure [13].

There are two well known theoretical ways to get a 3-dimensional NFL not emanating from QCPs, both based on local physics. The first is the two channel Kondo effect, requiring an exact balance between two screening channels [14]; which like a QCP could be thought of as a point of precise tuning. NFL behaviour for the two channel Kondo model has recently been seen above quadrupole ordering temperatures in a series of cubic Pr materials with non-Kramers doublet ground states [15], and in related dilute systems with small concentrations of Pr replacing Y [16], as well as in earlier studies of $Y_{1-x}U_xPd_3$ [17]. These local NFLs are predicted to have a temperature dependence of their electrical resistivity $\rho(T) - \rho(0) \propto \sqrt{T}$ and be sensitive to magnetic field [18]. The second way requires a range of single channel Kondo

energy scales extending to zero energy, generated by disorder [19], and results in an approximately T-linear resistivity. The non-Fermi liquid state we report in UAu_2 is robust over a wide range of magnetic field and has signatures that are too strong to be attributed to impurities. UAu_2 is also crystallographically well ordered with a low residual electrical resistivity, ruling out explanations based solely on chemical disorder. We also do not see the entropy release in magnetic field that would be expected for the usual two channel Kondo effect.

For MnSi, thermodynamic evidence of the NFL state at high pressure is restricted to measurements of the lattice constant [20, 21]. These show to leading order in temperature, a conventional behaviour of the thermal expansion $\alpha \propto T$ [20]. Here, the NFL we report in UAu_2 is manifest in thermodynamic measurements extending to very low temperature and unlike for β-$YbAlB_4$, this is in a fully magnetically ordered state.

UAu_2 is a little-studied heavy Fermion metal known to order magnetically at 43 K [22]. It has a simple AlB_2-type hexagonal crystal structure [23] comprising a vertical stacking of flat sheets of a triangular lattice of U atoms, separated by sheets of gold (Fig. 1a). The calculated paramagnetic band structure is shown in Fig. 1b (calculation details and band dispersions are given in the Supporting Information (SI)). The magnetic phase diagram and magnetic structure we find are shown in Fig. 1c. After discussing magnetic and charge ordering (Fig. 2) we present our thermodynamic and transport measurements showing NFL behaviour (Fig. 3-5), then discuss these and present our conclusions.

MAGNETIC PHASE DIAGRAM AND CHARGE ORDER.

Theoretically, a 2-dimensional triangular lattice with only nearest neighbour antiferromagnetic interactions adopts three-site order defined by the moment direction on three nearest-neighbour sites. The magnetic unit cell then has dimensions $\sqrt{3} \times \sqrt{3}$ compared with the atomic cell [24] (Fig. 1a). For an Ising magnet, where the moments are constrained to be parallel or antiparallel to a fixed direction, it is impossible to align adjacent moments on the three sites anti-parallel, leading to the phenomena of geometric frustration with a ground-state degeneracy that depends exponentially on the system size, giving a finite ground state entropy per volume. The inclusion of higher than quadratic-order spin fluctuations in the antiferromagnetic Ising-Heisenberg model [25] or of interactions that have a range beyond nearest-neighbour [26] lifts this degeneracy. The low temperature state, is then predicted to be ferrimagnetic with spins on three nearest neighbour sites $\{\uparrow, \uparrow, \downarrow\}$ [27, 28]. A partially ordered $\{\uparrow, \downarrow, 0\}$ state may occur at higher temperature where higher entropy states are favoured [29]. In UAu_2, the triangular lattice is stacked along the third direction forming columns of U-atoms. Isostructural materials are known to exhibit a wide range of complex magnetic structures [30].

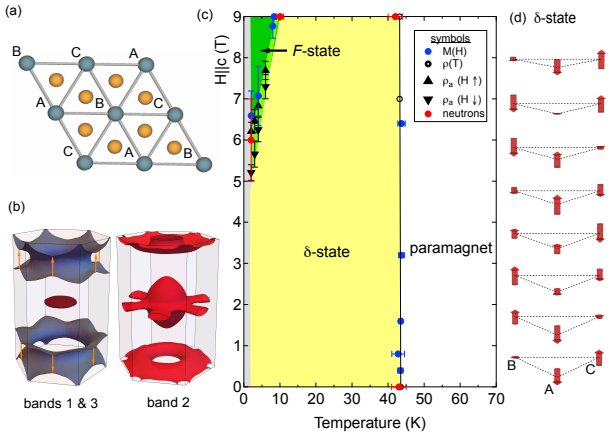

FIG. 1. (a) The crystal structure of UAu_2 viewed along the c-axis showing 2 x 2 unit cells in the ab plane. Au atoms (coloured gold) are at $c = 1/2$ and U atoms (blue) are at $c = 0$. There is only a single crystallographic inequivalent site for each atom. The U atoms lie on a triangular lattice in the plane. In the magnetic unit cell, U atoms in the plane labelled A,B and C are no longer equivalent to each other. Geometric frustration occurs for Ising moments with antiferromagnetic nearest neighbour interactions. To see this, consider the case where the A-sites have spin ↑ and C have spin ↓; the energy is then the same for either choice of spin direction at every B site. (b) The calculated Fermi surface. The "crown" in blue is a hole band (band 1), the "button" (maroon) is an electron band (band 3). Band 2 has two electron pockets, the "propeller" at the zone centre and the "doughnut" at the zone edge. The orange arrows connecting menisci of the crown are nesting vectors $(0, 0, 0.14)$ responsible for a peak in the static Lindhard function. Band dispersions and the density of states, decomposed into orbital contributions are shown in SI Fig. S1. (c) The temperature - magnetic field phase diagram determined from our measurements of intermediate and high quality single crystals. The transitions are detected in magnetisation measurements (M), resistivity (ρ) and with neutron scattering (see the SI for details). In the ferrimagnetic state (F-state) $A =\uparrow$, $B =\downarrow$ and C is aligned with the magnetic field with no modulation along the c-axis. The ordered state that occupies most of the figure is incommensurately modulated along the c-direction (δ-state). This magnetic structure is shown in (d) which depicts 7 unit cell-lengths along the c-direction (vertical). The moments (red arrows) are $\vec{m} \propto \vec{c}\cos(2\pi\delta.z + \theta)$. The phase angle θ differs by $\pm 2\pi/3$ between adjacent columns. In the region labelled δ-state a small trace of the F-state was still found. For high-quality crystals the corresponding volume fraction was below 0.6%.

We performed elastic neutron scattering measurements on a finely powdered sample and individual single crystals from two Czochralski growths to determine the magnetic order in UAu_2. The experimentally determined temperature - magnetic field phase diagram for field $H \parallel \mathbf{c}$ is shown in Fig. 1c. At low temperature (2 K)

a magnetic field above 6 T (along the c-axis) induces a strongly polarised commensurate $\sqrt{3} \times \sqrt{3}$ state with Bragg peaks at $(\frac{1}{3}, \frac{1}{3}, 0)$ (reflection indices are given relative to the crystal structure). This state is identified as the ferrimagnetic state $\{\uparrow, \uparrow, \downarrow\}$ with no modulation along the columns (hereon referred to as the F-state). The ordered uranium moments have magnitude $\sim 1.0\ \mu_B$, deduced from magnetometer measurements and the neutron data. In the rest of the letter we focus on the δ-state formed in lower field. This state exists alongside a residual fraction of F-state. For high quality single crystals the volume fraction of F-state at zero field is less than $\sim 0.6\%$ over the complete temperature range studied. A more significant volume fraction of powdered and polycrystalline samples transform to the F-state at low temperature in zero applied field, most likely as a result of internal strain. A comprehensive description of the fraction of F-state and sample quality is provided in the SI.

The δ-state is a $\sqrt{3} \times \sqrt{3}$ magnetic state that is sinusoidally modulated along the c-direction with magnetic Bragg reflections at $(\frac{1}{3}, \frac{1}{3}, \delta)$. The modulation period δ is incommensurate with the lattice and changes continuously from $\delta \sim 1/8$ at T_N to $\delta \sim 0.138$ at 2 K (Fig. 2b) and is insensitive to magnetic field along $\mathbf{c}$. The magnetic moments are aligned with the c-axis (see SI). This is consistent with the magnetic susceptibility, which shows a much more pronounced kink at T_N in the c-axis component than for the a-axis (SI Fig. S6), and the near vertical transition line between the δ-state and paramagnetic state in the magnetic-field temperature phase diagram (Fig. 1c). The magnetic moments on the three sites in a triangle have to sum to zero at all temperatures in the δ-state, since any ferrimagnetic component would lead to additional reflections such as $(1, 0, \delta)$ where no intensity was seen.

States consistent with the above observations can be built from any combination of two states, one with the phase of the modulation differing by $2\pi/3$ between neighbouring columns $A \rightarrow B \rightarrow C$ (Fig. 1d) denoted δ_+, and the other with phase differences of $-2\pi/3$, denoted δ_-. The transition from δ to F induced by an applied field is strongly first order (hysteretic) and accompanied by a sharp drop in the electrical resistivity (SI Fig. S7). The δ-state in UAu_2 is similar to the magnetic state observed below T_N in the rhombohedral insulator $Ca_3Co_2O_6$ [31]. However, at lower temperature the magnetic structure in $Ca_3Co_2O_6$ transforms slowly to an antiferromagnetic striped state that no longer preserves the $\sqrt{3} \times \sqrt{3}$ arrangement [32].

We performed zero-field X-ray scattering measurements on the same single crystals studied with neutrons. Resonant scattering at the U M_4 edge identified the same magnetic peaks seen with neutrons in the δ-state and azimuthal scans with polarisation analysis confirmed the moments are directed along the c-axis. We also made measurements with 11.2 keV X-ray photons and a much higher X-ray intensity. These measurements revealed

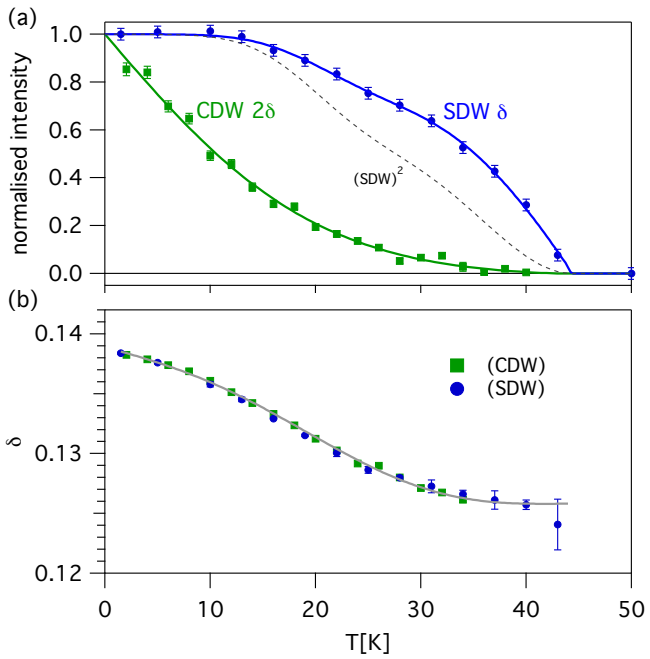

FIG. 2. (a) The zero-field temperature dependence of the SDW and CDW amplitudes squared, normalised to their values at low temperature, proportional to the integrated neutron and X-ray scattering at Bragg peaks with modulation vectors δ (neutrons, SDW) and 2δ (X-rays, CDW). Both neutron and X-ray measurements were performed on the same high-quality single crystals that contained less than 0.6% of the high field F-state (see SI). The lines through the points are guides to the eye. The SDW amplitude clearly saturates at low temperatures below 15 K and has a globally convex shape which are conventional features. In contrast, the CDW amplitude continues to grow with decreasing temperature at the lowest temperatures and has a concave shape. The dashed line shows the square of the SDW intensity, which is the expected form for a charge modulation due to magnetostriction. The CDW in UAu_2 clearly has a very different temperature dependence showing that it is not principally caused by magnetostriction. (b) Shows that the value of δ is the same for both the CDW and SDW (the line is a guide to the eye).

the presence of charge peaks below T_N at $(\frac{1}{3}, \frac{1}{3}, 2\delta)$ and equivalent positions. The identical temperature dependence of $\delta(T)$ for the charge density modulation (charge density wave, CDW) and the magnetic modulation (spin density wave, SDW) show they are related (Fig. 2b). A careful search was made at 2 K and close to T_N for diffraction peaks at $(\frac{1}{3}, \frac{1}{3}, 0)$ and related positions; none were found. Given that the CDW is linked to the magnetic structure, peaks at these positions would be expected for magnetic states made from superpositions of opposite helicity δ_+ and δ_-. The absence of these peaks, therefore, implies that locally the δ-state is pure δ_+ or δ_- at both temperatures. This rules out an entropy driven transformation to a partially ordered state. To see if we could understand the origin of the magnetic δ-structure, we examined a simple theoretical model with

fixed Ising moments. For long range exchange parameters along the c-axis that fix the period of the modulation and a weak nearest neighbour antiferromagnetic exchange in the plane, we confirmed that the spin arrangement observed experimentally and shown in Fig.1d minimises the free energy (see SI). The modulation along the c-axis may result from nesting features of the Fermi-surfaces (Fig. 1b).

We found no evidence for higher harmonics of the SDW or CDW order that would accompany a squaring up of the modulation in either the neutron or X-ray studies (SI Fig. S9 and S10). The temperature dependence of the intensity of the SDW and CDW are shown in Fig. 2a. A charge density wave at $q = 2\delta$ can be induced by magnetostriction, as found for the SDW in chromium [33] with charge peak intensities proportional to the square of the magnetic intensities and with additional higher multiple CDW harmonics at $q = 2n\delta$ (for integer n). In contrast, the temperature dependence of the CDW for UAu_2 is not a simple power of the magnetic intensity $I_{\rm SDW}$ (Fig. 2a) and there are no higher harmonics. While the magnetic intensity changes very little below $T^* \sim 15$ K, the intensity of the CDW in UAu_2 increases strongly as the temperature is reduced below T^*, with a strong temperature dependence down to the lowest temperature measured (2 K). Combined CDW/SDW order with a charge modulation vector that is twice the magnetic modulation vector has also been reported in stripe phases [34] in cuprate superconductors and closely related nickelates. In these systems, rivers of high charge density act as anti-phase domain boundaries between antiferromagnetic regions. But unlike in UAu_2, the charge ordering is always observed at a higher temperature than the magnetic ordering, characteristic of a transition that is driven by charge [34]. For UAu_2, the CDW develops below the magentic ordering temperature suggesting it has a different origin from the cuprates. The strong low temperature dependence suggests the CDW may be linked with the non-Fermi liquid behaviour that we describe next.

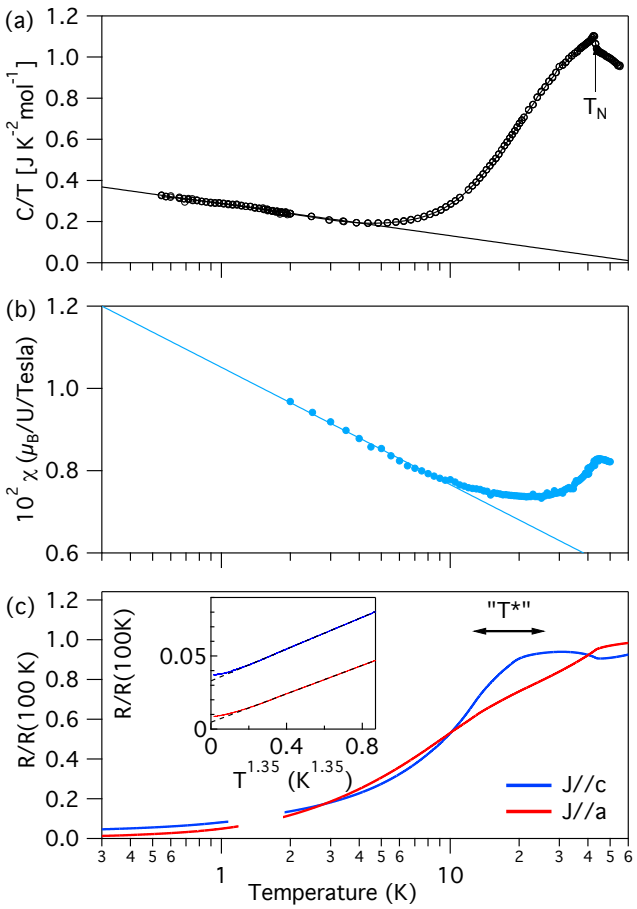

FIG. 3. Low temperature macroscopic properties of UAu_2 in zero field. The main panels show (a) the heat capacity divided by temperature C/T, (b) the susceptibility χ and (c) the resistivity ρ plotted against temperature on a logarithmic scale. There are clear signatures at the magnetic ordering temperature $T_N = 43$ K and a cross-over in behaviour around $T^* \approx 20$ K. In (a) the solid line shows a fit to $A - B\log(T)$ between 0.5 and 4 K. In (b) the solid line is a fit to $A - B\log(T)$ for $T < 9$ K. In (c) the resistivity is normalised to the value at 100 K. The inset shows the low temperature resistivity against $T^{1.35}$. The straight dashed lines indicate the $T^{1.35}$ dependence persists to ~ 300 mK. A gradual increase in the exponent of resistivity to T^2 occurs below 300 mK. All measurements were performed on high-quality single crystals that contain less than 0.6% of the high field F-state (see SI).

THERMODYNAMIC AND TRANSPORT MEASUREMENTS

We find the heat capacity has a non Fermi-liquid behaviour $C/T = A\log(\Theta/T)$ with $A = 68$ mJ mole^{-1}K^{-2} and Θ=69 K (Fig. 3a) over at least a decade in temperature below 4 K. Other contributions including from phonons make it difficult to determine an upper limit above 4 K. A natural temperature scale over which this behaviour might persist is deduced from the c-axis resistivity, which shows a decrease in slope in the range 10-20 K (Fig. 3c) and the susceptibility that starts to increase with decreasing temperature in the same temperature range (Fig. 3b). The change in entropy due to the $\log(\Theta/T)$ term between 0 K and 20 K equates to $0.5R\log(2)$ per uranium. The low temperature differential susceptibility in the δ-state follows $\chi(0) - \chi(T) \propto \log T$ (Fig. 3b). The ratio of the coefficients of the $\log(T)$ terms for C/T (in units of JK^{-2}mole^{-1}) and χ (in units μ_B/Tesla) is close to the Wilson ratio $(\pi^2/3)(Rk_B/\mu_B)$. The non-Fermi liquid behaviour is therefore consistent with a renormalisation of the quasiparticle effective mass. This contrasts with the case of β-$YbAlB_4$ where the Wilson ratio diverges towards low temperature, consistent with strong and increasing ferromagnetic fluctuations with decreasing temperature [12].

The heat capacity measured at very low temperature

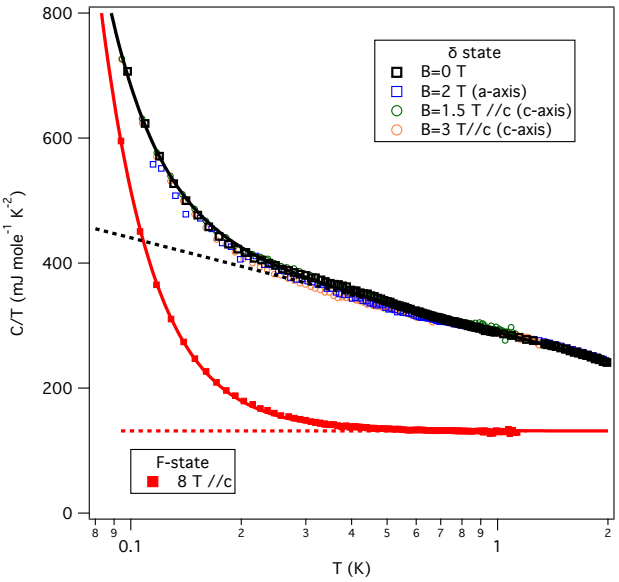

FIG. 4. Temperature dependence of the the heat capacity divided by temperature for high quality single crystals of UAu_2 at low temperature. There is only a very weak magnetic field dependence of the heat capacity for fields of a few Tesla in this temperature range, where the sample is in the δ-state. The solid line is a fit at zero field to $C/T = a/T^3 + b - c\,\log(T)$ (a, b and c are constants). The first term in this expression arises from the nuclear hyperfine states of gold and uranium nuclei (see SI for details). The dashed line shows the electronic contribution from the other two terms. A $\log(T)$ behaviour is characteristic of a non-Fermi liquid. For a field $H \parallel c = 8$ T the sample is transformed into the commensurate ferrimagnetic F-state (the high-quality single crystals studied have less than 0.6% of the F-state present in the δ-phase (see SI)). The temperature dependence in this case is $C/T = a'/T^3 + b'$ (solid line). There is no $\log(T)$ term and the electronic contribution is constant (dashed line), characteristic of a normal Fermi liquid. For intermediate c-axis fields the sample transforms abruptly and hysteretically between the two states. Some crystals have an additional bump in C/T of height less than 20 mJ mole^{-1} K^{-2} located in the temperature range 300-500 mK with a sample dependent width (see SI Fig. S3). The bump is suppressed with field and absent in fields of several Tesla. The sample dependence of this feature suggests that it has an extrinsic origin (see SI). It makes an insignificant contribution to the entropy compared with the $\log(T)$ term.

is shown in Fig. 4. Gold nuclei have an extremely small dipole moment but significant quadrupole moment. This leads to a $C/T \sim 1/T^3$ quadrupolar Schottky contribution to C/T that dominates the heat capacity below $\sim$ 0.1 K. The electric field gradient at the gold site was calculated from the band-structure and splits the gold nuclear-levels into two doublets separated by $\Delta E/k_B \sim 9$mK. There is additionally a small contribution from ^{235}U (the depleted uranium in our samples contains $\sim 0.2\%$ ^{235}U), which also has a quadrupole moment. The observed magnitude of the $1/T^3$ coefficient may be fully accounted for by these terms (see SI for details). The strong Ising anisotropy of UAu_2 would mean any transverse spin-wave fluctuations are gapped, and therefore no T^3 contribution from magnons is therefore expected.

As well as the $\log(T)$ term and nuclear Schottky contribution in zero magnetic field, in some crystals there is a weak additional contribution to the heat capacity below 500 mK (SI Fig. S3) associated with only a very tiny change of entropy ($\sim 0.02R\log(2)$). Unlike the $\log(T)$ term, this extra contribution is suppressed in a small magnetic field and is attributed to defects (SI Fig. S3). No change in the magnetic Bragg peak intensity or modulation vector was seen in the δ-state between 1 K and 40 mK with neutron scattering, shown in SI Fig. S10, therefore, we can rule out any bulk magnetic transition at low temperature and zero field.

$C/T = A\log(\Theta/T)$ has only a very weak field dependence in fields of up to several Teslas, shown in Fig. 4. In field, after removing the $1/T^3$ contribution, $C/T \sim \log(1/T)$ appears to persist to the lowest temperature for which the Schottky term can be reliably subtracted ~ 0.1 K (SI Fig. S15). For larger fields along $\mathbf{c}$, above 4 T, the δ-state can be obtained by zero field cooling but is metastable and transits to the F-state abruptly and irreversibly as the temperature is increased. At 8 T, the sample is in the F-state irrespective of the field history and $C/T = \gamma$, is a constant, characteristic of a standard Fermi liquid (plus a $1/T^3$ nuclear Schottky contribution). Thus in summary, the δ-state has an electronic heat capacity $C/T \sim \log(1/T)$ dependence from ~ 0.1 K to above 4 K. The same dependence survives in magnetic fields of several Tesla.

The thermal expansion determined from the X-ray scattering measurements is shown in Fig. 5, where it is compared with that calculated from C/T and a temperature independent Grüneisen parameter, Γ. The consistency of the two curves below 10 K does not suggest any low temperature divergence of Γ.

We will now discuss the electrical resistivity. The low temperature resistivity of UAu_2 has a non-Fermi liquid $\rho(T) - \rho(0) \propto T^{1.35}$ dependence down to a temperature below $\sim$ 300 mK (inset Fig. 3c). Below this temperature there is a gradual increase in exponent that at the very lowest temperatures can be described by $\rho(T) - \rho(0) \propto T^2$, the expected dependence for a correlated Fermi liquid. This may indicate the energy scale for inter site coherence is $200 - 400$mK, or it may be a cross-over to another lower temperature regime. Analogous to the heat capacity, the NFL behaviour and the cross-over temperature in resistivity is insensitive to magnetic field in the δ-state (SI Fig. S8). The resistivity is distinctly different from that in the NFL of the partially ordered phase of MnSi, where the $T^{3/2}$ dependence exists to a much lower temperature [8, 9]. Based on the cross over in the resistivity, the $\log(T)$ term in C/T might also be expected to saturate at a low temperature below 300 mK. The analysis of C/T below 300 mK depends on

the accurate subtraction of the $1/T^3$ tail from the nuclear Schottky contributions. A modification of the nuclear contribution could potentially obscure the identification of such a saturation.

DISCUSSION

We now discuss possible explanations of our findings. In a metal, uranium usually has a valence somewhere between U^{4+} (electron configuration $5f^2$) and U^{3+} ($5f^3$). Crystal symmetry imposes that the lowest states of the former configuration have total angular momentum quantum number $J = 4$ and are split into 3 non-Kramers doublets and 3 singlets [35]. The non-Kramers doublets have a quadrupole moment, but can additionally carry a dipole moment. The lowest energy states for U^{3+} have $J = 9/2$ and are split by the crystal field into 5 Kramers doublets. The heat capacity in Fig. 2 would be exceeded if there was a Schottky contribution from the crystal electric field levels with a splitting less than ~ 40 K or a phonon term with a Debye temperature below ~ 170 K. It is however possible to accommodate within the measured heat capacity a Schottky term with a larger splitting as might arise from the CEF acting on U moments (and a larger Debye temperature). These contributions to the heat capacity are irrelevant below ~ 4 K, where $C/T \sim \log(1/T)$ is observed.

We now turn to discuss the origin of $C/T \sim \log(1/T)$; this particular dependence is referred to with the abbreviation MFL (marginal Fermi liquid) in the following. Although a rigid density of states with a 2D Van Hove singularity can give $C/T \sim \log(1/T)$, this cannot account for the magnitude of the constant of proportionality observed and would be sensitive to magnetic field.

An explanation based on the proximity to a QCP between the δ-state and high field F-state can be ruled out; the field induced transition is strongly first-order, whereas a continuous transition is required for a QCP. Additionally, approaching the $\delta - F$ transition with increasing magnetic field does not lead to strengthening of the $\log(T)$ term in the heat capacity or an enhancement of the zero temperature T^2 contribution in the resistivity or a lowering of the cross-over temperature to $T^{1.35}$ (S.I. Fig. S8), all of which would be expected approaching a quantum critical transition.

For magnetically unordered ground states standard explanations for a MFL are based on a proximity to a magnetic quantum critical point (QCP). Considering only magnetic degrees of freedom a MFL is found for Hertz-Millis QCPs [36] between paramagnetism and either 3D FM or 2D AFM [37]. The key point is that this is restricted to temperatures above T_N. Below T_N the magnetic fluctuations linked to the order cannot give rise to quantum critical behaviour since the Fermion spectrum is gapped at the ordering vector and the only excitations within this gap are Goldstone modes that are undamped and cannot give the required divergence of the self-energy [38]. Thus, while there are many magnetically unordered materials that are MFLs, UAu_2 provides a unique example where such a behaviour is found within a magnetically ordered state. A different degree of freedom is therefore required to explain non-Fermi-liquid behaviour below T_N.

Quadrupole order, linked to a non-Kramers U^{4+} doublet single ion ground state, provides a natural candidate for a second degree of freedom. One possibility is that this degree of freedom is close to ordering at a QCP below T_N. $Ce_3Pd_{20}Si_6$ provides an example of the opposite case, where an AFM QCP occurs within a quadrupolar-ordered state [39, 40]. A proximity to a QCP can however be ruled out for UAu_2 from the thermal expansion below 10 K, shown in Fig. 5. Below 10 K the thermal expansion is proportional to the heat capacity, corresponding to a temperature independent Grüneisen parameter Γ. This contrasts sharply with a divergence of Γ that would be expected approaching a QCP. The same conclusion also applies to QCPs from extensions [41] of the Doniach phase diagram [42] or for a quantum critical valence transition [43]. While we have ruled out a QCP, the non-monotonic variation of the thermal expansion β_a between 10 and 20 K and a change in anisotropy from $\beta_c/\beta_a < 2$ below 10 K to $\beta_c/\beta_a \sim 10$ above 20 K, nevertheless suggest that valence changes occur away from zero temperature. The temperature dependence of the CDW and SDW intensities and resistivity all show changes in this temperature range, the origin of which remains an open question.

Without magnetic order, a non-Kramers U^{4+} doublet ground state can form a two-channel Kondo state [44] (2CK) giving a MFL. Indeed, the calculated 2CK heat capacity [45, 46] scaled to the lattice density of UAu_2 can reproduce the measured low temperature heat capacity well (SI Fig. S15a). The zero temperature residual entropy $0.5R\log(2)$ inherent in the 2CK state, is however, released on a temperature scale T_s when the degeneracy of the two channels is broken. The degeneracy is broken by an effective field [47] coming from both magnetic order and an applied field. A field of a Tesla would give an easily visible increase of C/T (a detailed calculation is given in the SI). Such an increase is not seen experimentally, implying a uniform two channel Kondo state does not provide a straightforward explanation for our findings. We now examine whether the entropy release due to the magnetic order itself may result in a MFL.

The incommensurate nature of the modulated order means that there will be some ions that are located close to nodes of the total effective field comprising the sum of the field due to the modulated order and applied field. The two channel Kondo analysis could still apply for these sites. For the sample as a whole, incommensurate order will result in a distribution of temperature scales T_s over which the 2CK residual entropy is released, with T_s extending down to zero temperature at the nodes. A MFL would result if the distribution of T_s values was constant as $T_s \to 0$, or more precisely constant to below

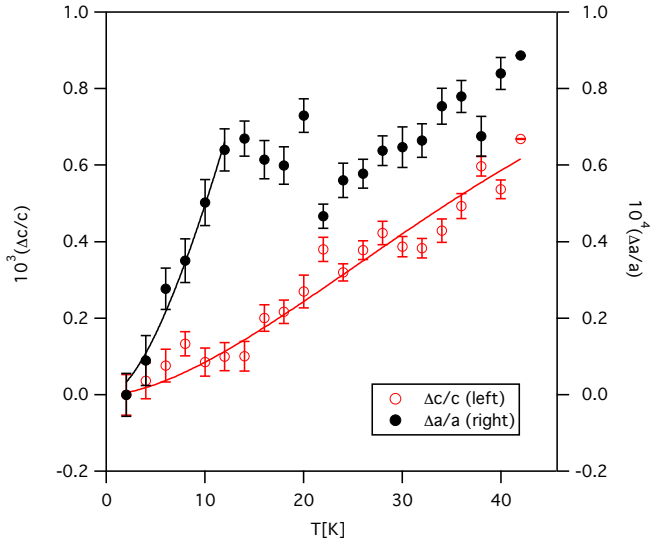

FIG. 5. The relative change in the **a** and **c** lattice parameter as a function of temperature in zero field deduced from X-ray diffraction for the (3,0,0) and (3,0,1) diffraction peaks of high-quality single crystals that contain less than 0.6 % of the high field F-state. The solid lines are fits to $\Delta a \propto \Delta c \propto \int C(T)dT$, with $C/T \sim \log(69/T)$ (the only free parameter is a constant of proportionality for each direction). This analysis is valid for a constant Grüneisen parameter.

the lowest temperature measured (SI Fig. S15b). This idea is similar to one used to explain a MFL and linear in temperature resistivity in $Th_{0.93}U_{0.07}Ru_2Si_2$ [48], based on a distribution of single-channel Kondo temperatures [19, 49] (in that case the distribution was attributed to chemical disorder). We now briefly consider the distribution of T_s predicted theoretically. In the 2CK model T_s is proportional to the square of the difference of the coupling strength for the two screening channels. For an isolated ion and no order this results in $T_s \propto H^2$ where H is the magnetic field [47]. This relation and a sinusoidal spatial variation for H due to magnetic order, does not give the required flat distribution of T_s ($T_s \propto H$ is required for this). A related problem was encountered when trying to explain the field dependence of the susceptibility and C/T in $Th_{0.93}U_{0.07}Ru_2Si_2$ starting from the 2CK model. To get $T_s \propto H$ for $Th_{0.93}U_{0.07}Ru_2Si_2$, models start from more complex crystal field schemes such as the accidental degeneracy of two singlets [50], or a combination of a non-Kramers doublet and two singlet levels [51, 52]. These models move the sweet spot field at which the balanced 2CK response occurs from zero field to a finite field. The field distribution from the incommensurate order plus an applied field could continue to encompass the sweet spot over a wide range of applied fields. This would naturally explain the resilience of the MFL in applied field. Also, since there is no longer a continuous field distribution in the F-state, which is not modulated, this would also naturally account for the disappearance of the MFL. None of the above analysis considers coherence between Kondo sites, which is a formidable theoretical challenge, but essential to explain, for example, the behaviour of the electrical resistivity.

CONCLUSIONS

Although its crystal structure is incredibly simple, UAu_2 has very unusual properties. The triangular lattice is a well known source of magnetic frustration and UAu_2's Néel temperature is indeed less than the magnitude of its Curie-Weiss temperature (see SI), consistent with a modest suppression of the ordering temperature due to frustration. The low temperature magnetic structure we report is unique to UAu_2, but we have shown it can be accounted for in a straightforward way. Frustration in this case resists the tendency for the modulation to square up as the temperature is reduced, so that other mechanisms that stabilise or quench the remaining fluctuating moments, such as Kondo screening have an increased opportunity to play a role. At temperatures well below T_N, we found a non-Fermi liquid heat capacity, that is surprisingly robust in magnetic field. Frustration and potential valence fluctuations invite comparisons with the NFL in β-$YbAlB_4$ [12], however, the presence of magnetic ordering and robustness in magnetic field, clearly distinguish UAu_2 from β-$YbAlB_4$. Additionally, below T_N a charge modulation was detected that is locked to the magnetic order, but cannot be explained by simple magnetostriction. The intensity of charge modulation increases dramatically at low temperatures mirroring the non-Fermi liquid C/T, suggesting that these two features may be related. Charge transfer connected with the Anderson impurity description of Kondo physics is well established theoretically [53, 54], but has not, as far as we are aware, been observed experimentally in bulk materials. The incommensurate long period nature of the magnetic order in UAu_2, however, means that this transfer may be observed in our case via diffraction, which coherently amplifies the signal affording a possible explanation of the CDW we observe. The lack of saturation of the charge signal with decreasing temperature is then direct evidence for a range of Kondo scales T_s, extending to zero temperature, that would also explain $C/T \sim \log(T)$. The range is inherent to the modulated magnetism and does not necessarily require chemical disorder. While encouraging, this analysis does not include the coherence between Kondo sites and requires further development to account for the actual distribution of T_s. Our findings show that UAu_2 forms an unusually robust non-Fermi liquid state in a clean material with a high RRR that is not anchored to a QCP. The simplicity of the material, makes it more amenable to study than other 3D systems such as non-Fermi liquid states in high T_c superconductors, where QCPs are also present, and MnSi, where a robust non-Fermi liquid state is only attained at high pressure.

MATERIALS AND METHODS

Samples of UAu_2 were obtained by Czochralski method with a rotating tungsten seed from a RF-levitated stoichiometric molten mixture of electro-transported depleted uranium (Ames laboratories) and high purity gold (99.999% Au, Alfa Aesar) from a water-cooled high conductivity copper crucible under a purified argon atmosphere. Single-crystalline grains within the sample were identified with Laue X-ray diffraction and cut with a spark eroder. Measurements of resistivity were performed by the standard four-point method on a Cryogenics Ltd CCR (2-300 K) and Cryogenics Ltd / Leiden dilution refrigerator (0.05-1.4 K). A Quantum Design MPMS Magnetometer was used to measure magnetisation in fields up to 7 T and a PPMS to measure heat capacity above 500 mK. Heat capacity measurements between 0.1-1.1 K in Fig. 4 were performed by the relaxation method in a dilution refrigerator. Time-of-flight neutron diffraction data were taken on the WISH time-of-flight diffractometer at ISIS, RAL, UK on both powder and single crystals. Resonant and non-resonant X-ray measurements were made at the XMaS BM28 beamline at the ESRF, Grenoble, France. Further details on the experimental methods and materials are given in the SI.

Acknowledgements We acknowledge support from the UK EPSRC grants EP/P013686/1 and EP/R013004/1.

SUPPLEMENTARY INFORMATION

METHODS

Sample preparation

Samples of UAu_2 were grown by the Czochralski method with a rotating tungsten seed from a RF-levitated stoichiometric molten mixture of electro-transported depleted uranium (Ames laboratories) and high purity (99.999 %) gold contained by a water-cooled oxygen-free high-conductivity copper crucible under a purified argon atmosphere. Single crystals were identified with Laue X-ray crystallography and extracted with spark erosion and additionally annealed under ultra-high vacuum at 850 C for 5 days. Samples were stored under vacuum to avoid oxidation in air.

Resistivity, magnetisation, specific heat and magnetoresistance measurements

Measurements of resistivity were performed by the standard four-point method with a Cryogenics Ltd CCR (2-300 K) and Cryogenics Ltd / Leiden dilution refrigerator (0.05-1.2 K). A Quantum Design MPMS Magnetometer was used to measure magnetisation in fields up to 7 T.

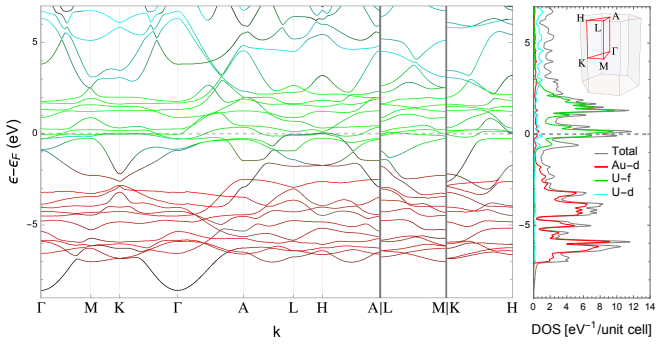

FIG. 6. Band structure and DOS for paramagnetic UAu_2, from DFT+U calculations. The projections onto Au d, U d and U f states are shown in red, turquoise and green respectively. The total DOS is grey. The inset shows the different directions in the Brillouin zone along which the band dispersions are plotted.

The susceptibility reported in Fig. 3 (main text) is the differential susceptibility in the field range 0.2-0.8 T (i.e. $[M(0.8) - M(0.2)]/0.6$); the minimum field value is high enough to avoid a contribution from ferrimagnetism (see below) and 0.6 T is well below the metamagnetic transition field. The heat capacity in the range 0.5-300 K at zero field was measured with a Quantum Design PPMS and in the range 0.08-3 K with and without magnetic field in a home built set-up.

Neutron and X-ray measurements

Time-of-flight neutron diffraction data were taken on the WISH time-of-flight diffractometer [55] at ISIS, RAL, UK on both powder and single crystals. The powder sample comprised a 7 g polycrystalline ingot that was ground up in a glovebox under a controlled argon atmosphere and sealed in a vanadium sample can. Resonant and non-resonant X-ray scattering measurements were made at the XMaS, on the BM28 beamline at the ESRF, Grenoble, France. The SDW intensity in Fig. 2a (main text) is the integrated intensity of the $(\frac{1}{3}, \frac{1}{3}, \pm\delta)$ Bragg peaks for a single crystal measured with neutrons. The CDW intensity is the integrated intensity of $(4\frac{1}{3}, -1\frac{1}{3}, 2+2\delta)$ and $(3\frac{1}{3}, -\frac{2}{3}, 1+2\delta)$ Bragg peaks measured with 11.178 keV X-rays (non-resonant scattering). In each case the pairs of peaks gave consistent results and the mean intensity is shown.

BAND STRUCTURE CALCULATIONS

The ELK code [56] was used to calculate the band structure for the experimental UAu_2 crystal structure with lattice parameters $a = 4.76$ Å and $c = 3.11$ Å. The muffin-tin radii of U and Au were set to 1.54 Å

and 1.36 Å respectively, and the product of the average muffin-tin radius with the magnitude of the maximum plane-wavevector was set to 7.0. Self-consistent ground state calculations were performed on a grid of $10\times10\times15$ **k**-points, which was increased to $20\times20\times30$ for non-self-consistent calculations to determine the density of states (DOS) and Fermi surface. The PBE exchange-correlation functional [57] was used with spin-orbit interactions included, and corrections to the on-site Coulomb interaction between U $5f$-states was implemented using the DFT+U method [58]. From the band structures, we calculated the static Lindhard function in the paramagnetic state

$$\chi_{ij}(\mathbf{q}) = \sum_{\mathbf{k}} \frac{f_{i,\mathbf{k}+\mathbf{q}} - f_{j,\mathbf{k}}}{\varepsilon_j(\mathbf{k}) - \varepsilon_i(\mathbf{k}+\mathbf{q}) + \mathrm{i}\eta}. \quad (1)$$

The subscripts refer to the band indices (spin indices are implicit) enumerated in Fig. 1 (main text). The component Re $\chi_{11}(\mathbf{q})$ has a peak at $(0, 0, \delta_{\mathrm{BS}})$ with δ_{BS} dependent on the choice of the DFT+U parameters U and J. We parametrise the DFT+U correction in terms of a single inverse screening-length λ for the on-site Coulomb interaction [59, 60]. We chose λ such that $\delta_{\mathrm{BS}} \sim 0.14$ corresponding to the observed c-axis component of the ordering vector at low temperature. The resulting Fermi surface, with $\lambda = 2.75a_0^{-1}$, is shown in SI Fig. 1. This corresponds to the effective DFT+U parameters $U = 1.32$ eV (the onsite Coulomb repulsion averaged over uranium $5f$-levels) and $J = 0.41$ eV (averaged intra-ion exchange interaction between different $5f$ states). The corresponding band structure and density of states (DOS) are shown in SI Fig. 6 and indicate that the states at the Fermi energy are predominantly made up of uranium f states. There are 2.6 f-electrons/uranium below the Fermi-level, which corresponds to a uranium valence of $\mathrm{U}^{3.4+}$.

SAMPLE QUALITY

Single crystal samples contain a small volume fraction that is ferrimagnetic at low temperature and field. This fraction varied between samples and is therefore not an intrinsic property, but most probably associated with localised regions near defects. The zero field remanent magnetisation gives a measure of the ferrimagnetic fraction, which has a similar temperature dependence for all the single crystals measured (SI Fig. 7). We denote single crystals showing a zero field remanent ferrimagnetic magnetisation $M_0 > 0.001\mu_B/\mathrm{UAu_2}$ (typically $0.003\mu_B/\mathrm{UAu_2}$) at 2 K as being of intermediate quality and those with $M_0 < 0.001\mu_B/\mathrm{UAu_2}$ as high quality. No systematic relation between M_0 and differences in growth conditions or the degree of surface oxidation has been identified. The residual resistance ratio RRR, defined as the resistance at 300 K divided by that at low temperature gives another measure of sample quality. High quality samples have RRR > 50 for current I along the a-axis. The two bar samples measured in Fig. 3 (main text)

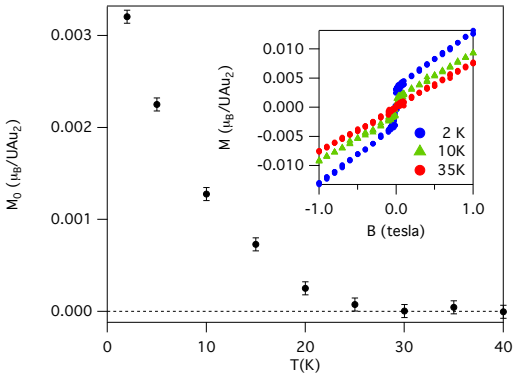

FIG. 7. The main figure shows the temperature dependence of the remanent magnetic moment M_0 deduced from hysteresis loop measurements for an intermediate quality crystal with the field along the c-direction. Hysteresis loops at different temperatures are shown in the inset. The remanent moment comes from a small volume fraction of the sample that is ferrimagnetic at low temperature and field. These measurements were made with a Quantum Design MPMS magnetometer.

were cut from the same crystal. The RRR and residual resistivity are 95 and 0.8 $\mu\Omega$ cm for $I \parallel \mathbf{a}$ and 35 and 1.0 $\mu\Omega$ cm for $I \parallel \mathbf{c}$. The low temperature resistivity is therefore close to isotropic compared with an anisotropy of the room-temperature resistivity ρ_a/ρ_c slightly above 2. Considerably higher RRRs and lower residual resistivities are obtained taking the low temperature resistance values (at high field) in the F-state.

The difference in quality between different high quality crystals does not affect any of the discussion in the main paper. The very low temperature heat capacity was measured for three different high quality crystals with RRR $\sim$ 73, $\sim$ 100 and $\sim$ 84, shown in SI FIG. 8. The measurements above 500 mK are indistinguishable. In addition to the $\log(T)$ dependence discussed in the main text, there is a small sample dependent contribution below 500 mK. It is peaked at 380 mK for the RRR $\sim$ 73 sample, at 420 mK for the RRR $\sim$ 100 sample and is practically absent for the RRR $\sim$ 84 sample. The sample dependence of this contribution and the small associated entropy are consistent with a non-intrinsic origin.

An ordering of the ^{235}U nuclear moments could provide a source of this contribution, with around the correct entropy. However, $\sim$ 400 mK would be an incredibly high temperature for nuclear moment order, despite the very large C/T connected with the non-Fermi liquid, which may provide an unusually strong electronically mediated interaction [61]. While the origin of this contribution has not been identified, the most likely source is magnetic defects.

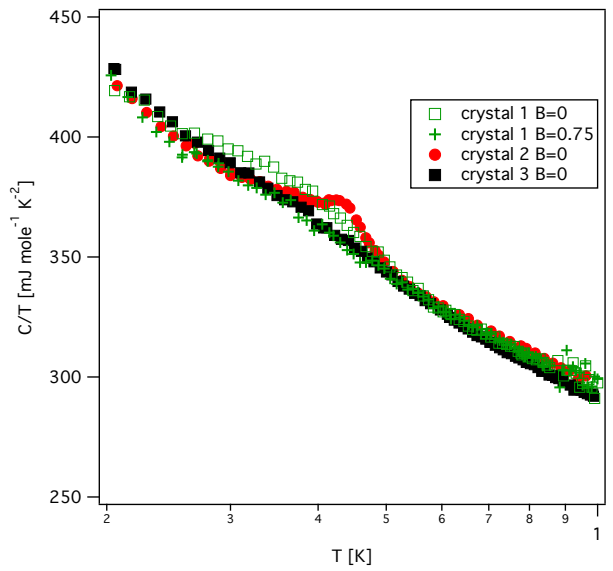

FIG. 8. C/T for 3 different single high quality crystals in zero field, with RRR 73, 100, 84 respectively. The first crystal shows an additional bump in C/T that is suppressed with field. The second crystal has a sharper bump. The third crystal has practically no bump. The presence of the feature is not clearly correlated with the RRR. Crystals 2 and 3 are adjacent parts of the same growth. The presence of this feature is therefore extrinsic. In Fig. 4 (main text) the data shown for $H = 0$ and $H \parallel a$ are for crystal 3, while the data for $H \parallel c$ are for crystal 1.

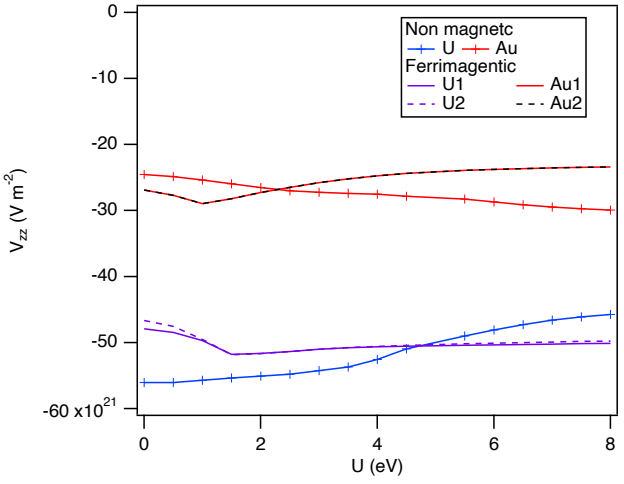

FIG. 9. The electric field gradient V_{zz} at each site calculated from DFT+U with no magnetic order and ferrimagnetic order, plotted as a function of the screening parameter U.

Schottky term calculation

Here, we provide the detail of our nuclear Schottky analysis that accounts for the very low temperature upturn of $C(T)$. The formula for the shift in nuclear energy levels due to a crystalline electric field is:

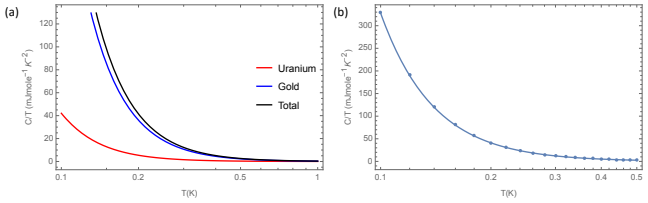

FIG. 10. (a) The calculated U and Au Nuclear quadrupole and their total contributions to the heat capacity. (b) The total contribution (points) compared with a $1/T^3$ term (line).

$$\Delta E = \frac{eQV_{zz}}{4I(2I-1)}\left(3M^2 - I(I+1)\right)\sqrt{1+\frac{\eta^2}{3}}. \qquad (2)$$

eQ is the quadrupole moment, $\eta = (V_{xx} - V_{yy})/V_{zz}$ with $V_{xx,yy,zz}$ the electric field gradients along the principle axes. I and M are the nuclear spin quantum numbers. The parameters for U and Au are given in Table S1 and Table S2 (below).

Isotope	abundance/UAu$_2$	Q(Barns)	I	μ/μ_N
Au^{197}	2	+0.55	3/2	0.15
U^{235}	0.002	+4.9	7/2	-0.38

TABLE I. Nuclear moment parameters (source [62]). Our samples contain depleted uranium, 0.2 % ^{235}U.

The mean of the maximum and minimum values for V_{zz} from our DFT calculations for a range of parameters is given in the following table and the values are plotted in SI FIG. 9. For the U sites $\eta = 0$ by symmetry. For Au $\eta = 0$ in the PM state and has a small value in the magnetically ordered states (its maximum magnitude is given in the table).

atom	V_{zz} (Vm^{-2})	±%	max$\|\eta\|$	Levels(mK)$^{\text{degeneracy}}$
U	-5.29×10^{22}	4	0	$(0)^2, (64)^2, (107)^2, (129)^2$
Au	-2.61×10^{22}	5	0.07	$(0)^2, (8.3)^2$

TABLE II. Potential gradients at U and Au sites calculated from DFT. Central values are given along with the spread covering both non-magnetic and ferrimagnetic states for screening parameter U in the range 2-4 eV. The resulting energy levels are given in the last column.

The heat capacity for these parameters is calculated from the partition function in the standard way. C/T is plotted for each contribution in SI FIG. 10(a). The total contribution is also compared with a single $1/T^3$ term in SI FIG. 10(b), giving an A coefficient of 0.33 mJ mol^{-1} K. The values of the A coefficient obtained experimentally in the F-state is 0.38 mJ mol^{-1} K at 8 T. This suggests that the DFT calculation provides a good description of the F-state. At low field in the δ-state the $1/T^3$ coefficient is

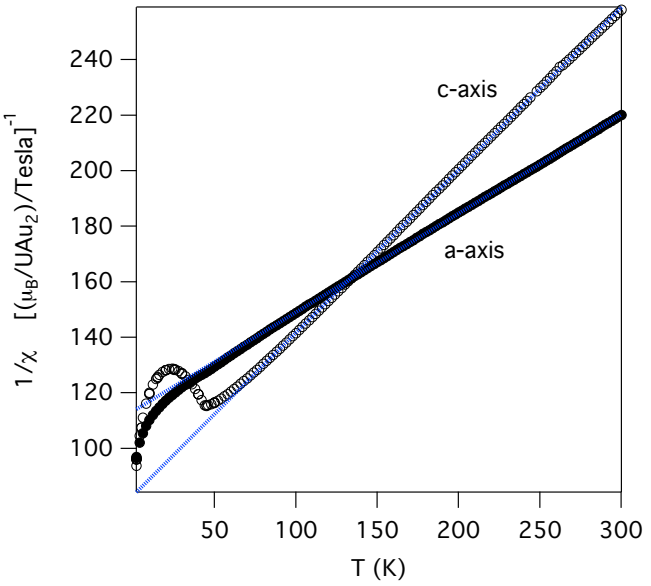

FIG. 11. The figure shows the inverse susceptibility H/B (with M in units μ_B/UAu$_2$ and B = 1 T) plotted against temperature. The dashed lines (blue) are straight line fits (Curie-Weiss Law) to the data in the range 80-300 K. The Curie-Weiss moments deduced from the straight line fits are $3.5\mu_B \parallel \mathbf{a}$ and $2.8\mu_B \parallel \mathbf{c}$ compared with the moment for a free U^{3+} ion of $3.6\mu_B$. The data shown is for a high quality single crystal; the same Curie Weiss moments and T_{CW} were found for an intermediate quality crystal.

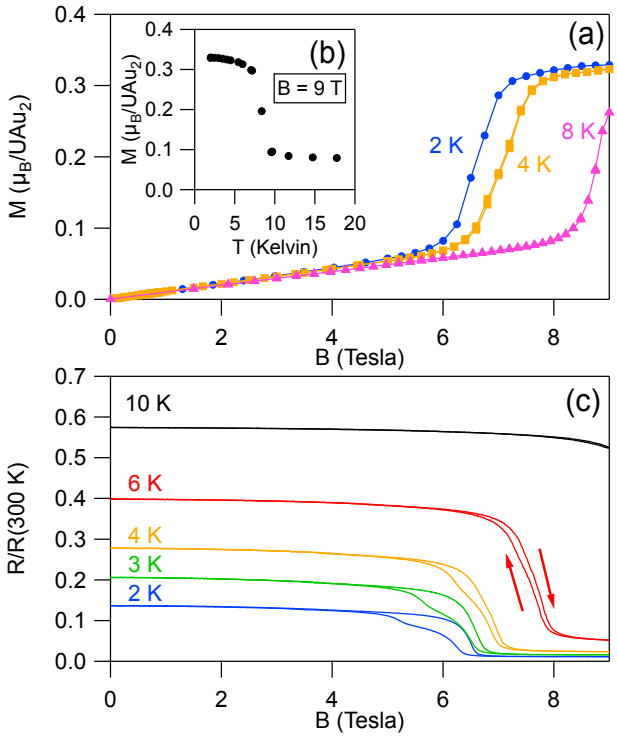

FIG. 12. Magnetisation (a) and (b), and electrical resistance (c), for applied magnetic field along the c-axis. The magnetisation measurements are on a high quality single crystal measured with a Quantum Design PPMS with vibration insert. Resistivity measurements are for a different crystal (similar transition fields and hysteresis were seen for several crystals). The transition fields (including hysteresis) shown in Fig. 1 (main text) are based on this data and the diffraction data in SI Fig. 14.

smaller ~ 0.24 mJ mole^{-1}K. This suggests that the DFT overestimates the electric field, with V_{zz} around 2/3 of the DFT estimate. The lower value compared with DFT in the δ-state may be explained by an enhanced screening of the electric field gradients in the non-Fermi liquid. A magnetic field of 10 T would give a dipole splitting less than ± 0.55 mK for Au and less than ± 1.4 mK for U, which are much less than the quadrupole splitting and two orders of magnitude smaller than $\sim$ 400 mK (the temperature of the small zero field peak in C/T).

Magnetisation, resistivity and magnetoresistance measurements

In the main text it is stated that above T_N the magnetisation of UAu$_2$ is almost isotropic with a paramagnetic Curie-Weiss behaviour. The supporting data is shown in SI Fig. 11. $T_N \sim 43$ K is much lower than the Curie-Weiss temperature 142 K indicating the presence of strong magnetic correlations that could be due to magnetic frustration.

The resistivity and magnetisation measurements used to construct the field-temperature phase diagram shown in Fig. 1 of the main text are shown in SI Fig. 12. The metamagnetic transition in the resistivity is seen in all the crystals studied (both high and intermediate quality single crystals).

For the non-Fermi liquid state, the resistivity below 1.5 K is well described by a power law $T^{1.35}$ down to $\sim$ 300 mK. Below this temperature there is a gradual increase in the exponent and $\rho = A + BT^2$ at the lowest temperature (main text Fig. 3(c)). The resistivity against $T^{1.35}$ at a series of fields in the δ-state for $J \parallel \mathbf{c}$ and $\mathbf{a}$, is shown in SI Fig. 13. The $T^{1.35}$ dependence is unperturbed by field and only a slight increase is seen in the temperature below which the exponent increases with field. The cross-over temperature rises and the T^2 coefficient falls with increasing field approaching the δ-F transition. This behaviour is the opposite of that expected approaching a QCP

The T^2 coefficient of the lowest temperature resistivity at zero field for $J \parallel c$-axis is 3.79 $\mu\Omega$cm/K^2. The low temperature heat capacity of 440 mJ/mol K^2 at 80 mK, shown in SI FIG. 20, gives a Kadawaki woods ratio of $R_{KW} = 19.6$ $\mu\Omega$ cm mol^{2}K^{2}J^{-2}, close to the value expected for heavy Fermion materials of $R_{KW} \sim 10$ $\mu\Omega$ cm mol^{2}K^{2}J^{-2} [63]. Extrapolating the heat capacity to ~ 4 mK gives $R_{KW} = 10$ $\mu\Omega$ cm mol^{2}K^{2}J^{-2}.

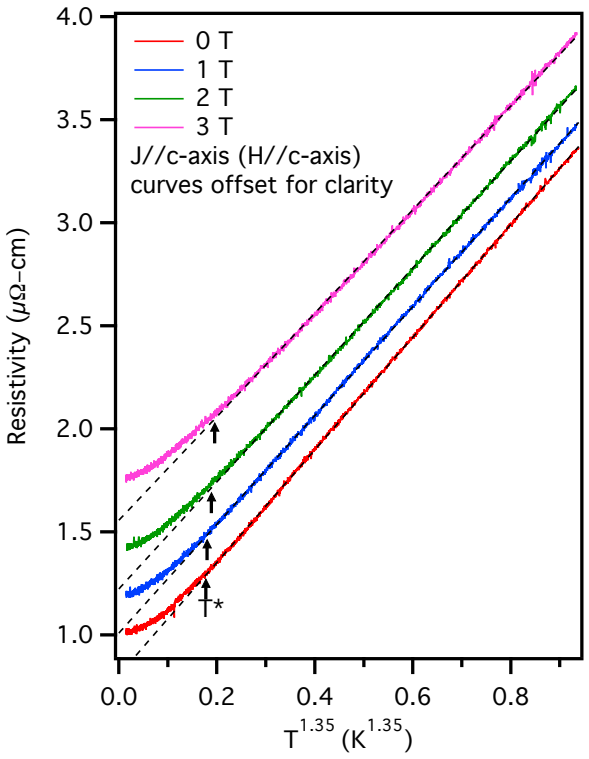

FIG. 13. The temperature dependence of resistivity at a series of fields for current (J) applied parallel to the c-axis. The resistivity shows a $T^{1.35}$ dependence to low temperature in the δ-state that is unperturbed by field, indicated by the straight dashed lines. At the lowest temperatures there is a gradual cross-over to an exponent of resistivity close to 2, expected for a Fermi liquid. The cross-over temperature is marked by arrows and only slightly increases with field.

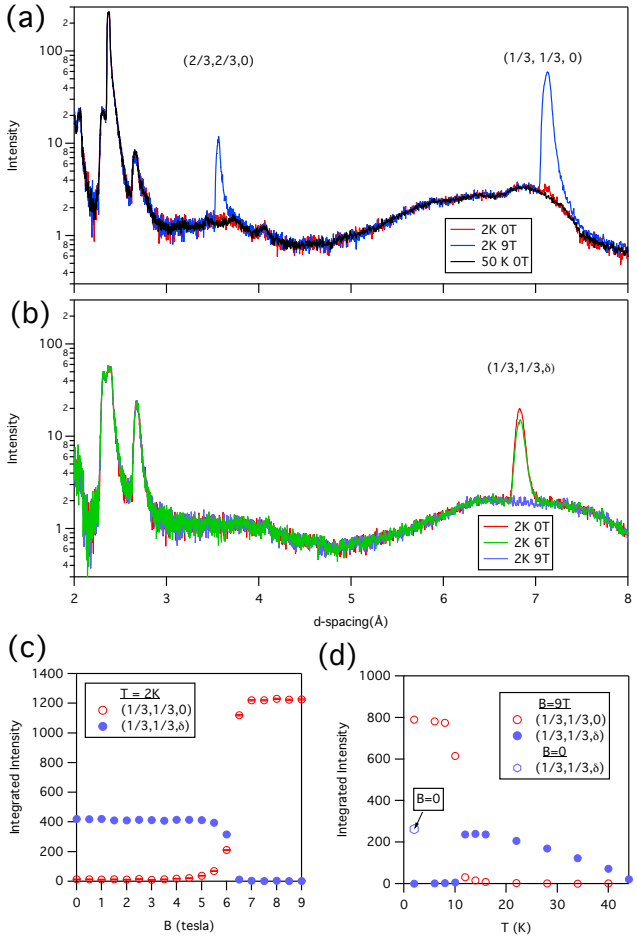

FIG. 14. The figure shows the scattering intensity integrated over angle for diffraction as a function of d-spacing (a) in the $(1/3, 1/3, 0)$ direction and (b) in the $(1/3, 1/3, \delta)$ direction. Measurements are shown for different temperatures and magnetic fields for a high quality single crystal. Panel (c) shows the integrated intensity of these peaks as a function of field at 2 K relative to the background intensity at zero field and 50 K. Panel (d) shows the relative intensity versus temperature at 9 T for a different piece of the same single crystal.

Single crystal neutron diffraction

SI Fig. 14 shows the single crystal diffraction spectrum for a high quality crystal at different magnetic fields and temperatures over two ranges of detector angles that cover the outgoing beam direction for the $(1/3, 1/3, 0)$ and $(1/3, 1/3, \delta)$ diffraction peaks respectively. The peaks at small d-values in the spectra are nuclear peaks and independent of field and temperature. It should be noted that unlike the F-state peak at $(1/3, 1/3, 0)$ the δ-state peak at $(1/3, 1/3, \delta)$ gives no 2^{nd} order signal at $d/2$, consistent with a pure sine-wave modulation. There is almost no intensity at the $(1/3, 1/3, 0)$ positions at low temperature and small field. The points in the temperature-field phase diagram (Fig. 1c main text) deduced from neutron scattering are deduced from the midpoints of the abrupt transitions seen in SI Fig. 14c and 14d.

Neutron scattering measurements in zero field were performed on high-quality single crystals down to 40 mK, shown in SI Fig. 15. No change in the modulation vector or intensity of the magnetic peaks is seen below 1 K down to 40 mK. This rules out the possibility of any low temperature magnetic transitions or a growth of harmonics that would arise if the modulation squared up.

Neutron powder diffraction

The neutron powder spectra at different temperatures are shown in SI Fig. 16.

The neutron powder diffraction data was analysed by the Rietveld method (with the FULLPROF programme [64]). For the nuclear and magnetic structure refinements, two out of the ten detector banks were excluded due to their comparatively large background signal. No Debye-Waller factor was used to avoid negative temperature factors. Three weak reflections were

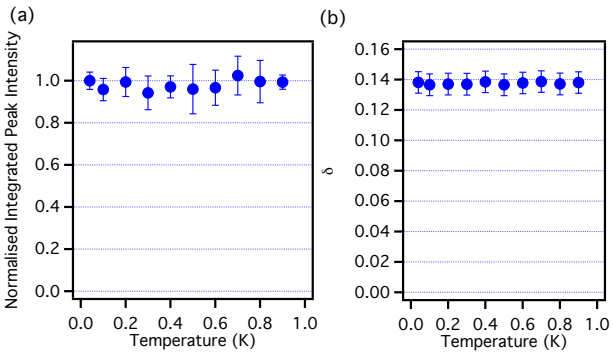

FIG. 15. (a) The integrated magnetic Bragg peak intensity below 1 K, normalised to the value at 40 mK. (b) The modulation vector δ below 1 K. Both quantities remain constant, with no indication of a magnetic transition.

observed at all temperatures which could not be indexed with the nuclear structure of UAu_2. One of these reflections arises from the vanadium sample can but the other two reflections are unidentified and may relate to a small quantity of impurity, possibly due to a small amount of surface oxidation of the powdered sample.

The reflections corresponding to both $\mathbf{q}_\delta = (h \pm 1/3, k \pm 1/3, l \pm \delta)$ (δ-state) and $\mathbf{q}_F = (h \pm 1/3, k \pm 1/3, l)$ (F-state) are of magnetic origin, highlighted by the lack of intensity at smaller d-spacings (larger q). A representational analysis performed with the SARAh software package [65] indicates that the irreducible representations (IRs) for possible magnetic structures have moments either completely along the c-axis or perpendicular to the c-axis. As discussed in the main text the moments are parallel to $\mathbf{c}$, supported by the absence of $\mathbf{q}_\delta$ and $\mathbf{q}_F$ reflections in the powder pattern with wavevectors having a significant c-component. This conclusion was confirmed by comparing Rietveld refinements for both choices of moment direction.

The valence of the U ions in UAu_2 is not known. Since the magnetic form factor for U^{3+} and U^{4+} are very similar, diffraction cannot be used to identify the valence state. The magnetic form factor in the dipolar approximation is $f(\mathbf{k}) \propto \mu(\langle j_0(\mathbf{kr})\rangle + \alpha\langle j_2(\mathbf{kr})\rangle)$, where the expectation values of the electron density weighted by the nth order Bessel functions $j_n(\mathbf{kr})$ are tabulated [66] as functions of the scattering vector $\mathbf{k}$, and μ is the total magnetic moment of the uranium ion. The magnetic structure refinements were performed with parameters for free U^{3+} ions with $\alpha = 1.63$ [67].

Different magnetic structures give identical fits for the $\mathbf{q}_F$ peaks. This includes structures with moments that sum to zero in the unit cell such as $\{\uparrow, \downarrow, 0\}$ as well as the ferrimagnetic structure $\{\uparrow, \uparrow, \downarrow\}$. The calculated magnetic diffraction for the latter structure also gives small intensities at nuclear reflection positions, such as $(1, 0, 0)$ that are, however, too small to be resolvable relative to the nuclear scattering in our measurements. A ferrimagnetic choice is required to explain the increase in the magnetic polarisation seen in the field induced phase at low temperature and the remanent extrinsic magnetisation. The structure $\{\uparrow, \uparrow, \downarrow\}$ is the simplest such choice, but there is no reason to set the magnitudes of the $\uparrow$ and $\downarrow$ moments equal. The resulting fit for the Rietveld refinement of the nuclear and magnetic structure for the powder diffraction data at 1.5 K for a mixture of δ-state and F-state is shown in SI Fig. 16.

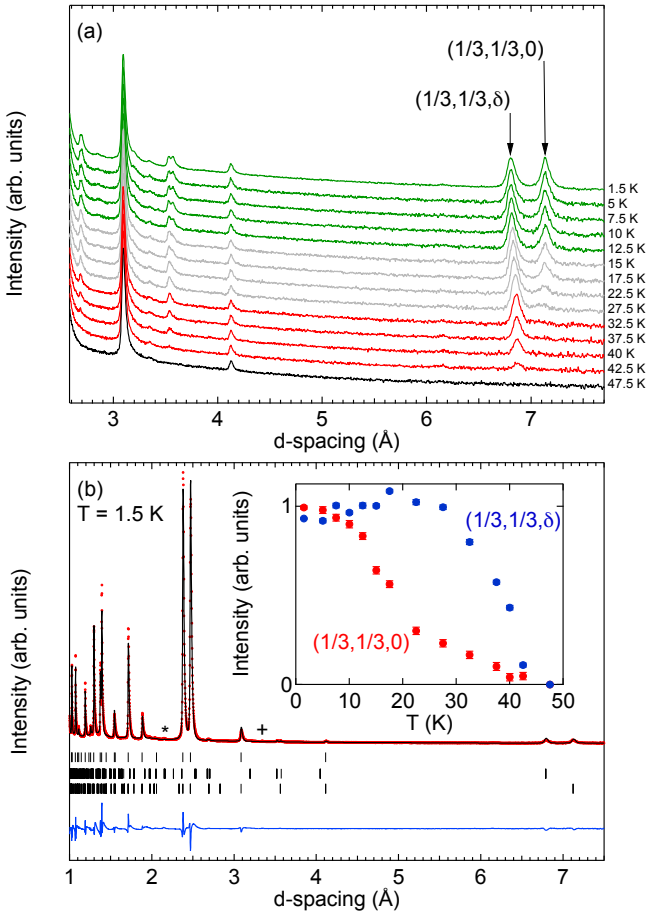

FIG. 16. Neutron Powder Diffraction. Panel (a) shows the measured powder diffraction spectrum as a function of d-spacing for different temperatures at large values of d where the magnetic diffraction peaks are prominent. The two largest d peaks have indices $(1/3, 1/3, \delta)$ and $(1/3, 1/3, 0)$. The value of δ is shown in Fig. 3b (main text). Panel (b) shows the data (points) over a wider range of d and the Rietveld fit (solid line) to the nuclear and magnetic structure at $T = 1.5$ K. The upper, middle and lower rows of vertical lines show the peak positions of the nuclear, $\mathbf{q_F}$ (F-state) and $\mathbf{q}_\delta$ (δ-state) reflections respectively. The asterisk indicates a reflection from the vanadium sample can, and the plus indicates an unidentified temperature independent reflection that might be from a small amount of impurity, for example due to oxidation. The lower curve shows the difference between the data and fit. The inset figure shows the intensity of the $(1/3, 1/3, \delta)$ and $(1/3, 1/3, 0)$ peaks as a function of temperature.

In order to estimate the temperature dependence of the

volume fraction of the F-state and the magnitude of the ordered moment it is necessary to know the amplitude of the F-state moments relative to the δ-state moment. SI Fig. 17 shows the volume fraction obtained if all the magnetic moment magnitudes are assumed to be equal. With this assumption, the magnitude of the low temperature moment is $\sim 1.0 \pm 0.05\ \mu_B$ and the ferrimagnetic fraction is 28% at 2 K. A similar volume fraction was found from the initial depolarisation in MuSR measurements on the same polycrystalline sample before it was ground to a powder [68].

It is clear from the increase of the the intensity at $(1/3, 1/3, \delta)$ with increasing temperature below 20 K (SI Fig. 17) compared with the almost flat dependence for single crystals with almost no F-state (Fig. 2a main text) that the F-state fraction transforms to the δ-state as temperature is increased.

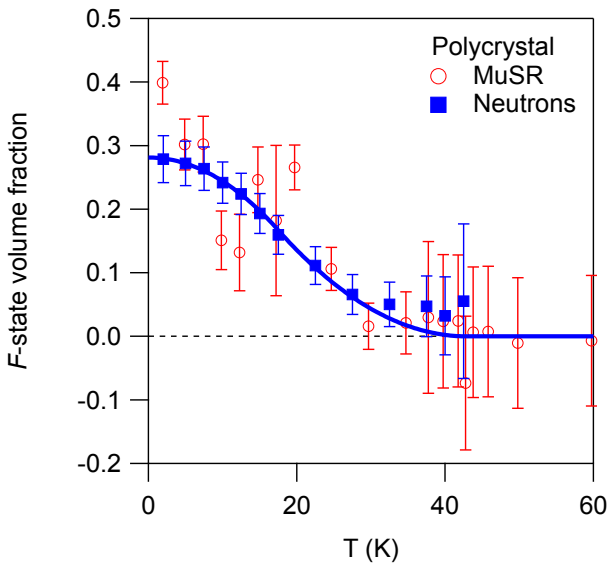

FIG. 17. The figure shows the volume fraction of a polycrystalline sample that has transformed to the F-state determined from the initial asymmetry in muon spin relaxation measurements and from neutron scattering. The line is a guide to the eye.

Fraction of F-state in the single crystals

The zero-field low temperature volume fraction of F-state in intermediate quality single crystals is estimated to be $\sim 2.7\%$ by comparing the ratio of the intensities of $(1/3, 1/3, 0)/(1/3, 1/3, \pm\delta)$ to the powder spectrum (taking account of the multiplicity factor for $\pm\delta$ in the powder data). The F-state remnant magnetisation in zero field is then $0.003\mu_B/0.027 \sim 0.11\mu_B/\mathrm{UAu_2}$. Comparison with the estimated magnitude of individual moments ($\sim 1\mu_B$) then suggests that for $\{\uparrow, \uparrow, \downarrow\}$ the $\uparrow$ moments are smaller than the $\downarrow$ moment. An applied field increases the magnitudes of the $\uparrow$ moments and reduces that of the $\downarrow$ moment, such that just above the meta-magnetic transition the state has a net moment $\sim 0.33\mu_B/\mathrm{UAu_2}$ (SI Fig. 4).

In zero field, the low-temperature intensity ratio $(1/3, 1/3, 0)/(1/3, 1/3, \pm\delta)$ for high quality single crystals is over a factor of 4 smaller than for the intermediate quality crystals implying a low-temperature zero-field F-state fraction $\sim 0.6\%$.

The temperature dependence of the $(1/3, 1/3, 0)$ intensity in the F-state for the single crystals differs from the powder sample and is very similar to the dependence of M_0 (SI Fig. 7). For the powdered sample the intensity, as well as being much stronger, appears to saturate at low temperature and has a tail extending to T_N.

THEORETICAL BACKGROUND FOR THE δ-STATE

A minimal Ising model requires the exchange couplings shown in SI Fig. 18a. These comprise long range couplings $J_c(q)$ along the c-direction peaked at $q = 2\pi\delta$ with δ the modulation wavevector (measured in reciprocal lattice units) and an antiferromagnetic nearest-neighbour exchange J in the ab-plane, which is sufficient to give the observed three sub-lattice structure. Other couplings between the chains are neglected, but are not expected to qualitatively change the results. We assume a simple form $J_c(q) = J_0 \exp[-(|q| - 2\pi\delta)^2/b^2]$ with a small value for b (SI Fig. 18b), consistent with strong Fermi-surface nesting along $\mathbf{c}$.

In the following we use a modulation wavevector of $\delta = 1/8$, commensurate with the lattice, in order to facilitate mean-field and Monte Carlo calculations on finite clusters. This value of δ, is very close to the experimentally observed modulation slightly below the transition temperature $T_N \approx 43$ K. To accommodate the three sublattice structure, we use systems with $3n_a \times 3n_b \times n_c$ lattice sites, subject to periodic boundary conditions (n_a, n_b, n_c are integers).

Mean-field analysis

In terms of the average local magnetisation $m_{\mathbf{r}} = \langle \hat{S}^z_{\mathbf{r}} \rangle$ the mean-field free energy is given by

$$F_{\mathrm{MF}} = \frac{1}{2} \sum_{\mathbf{r},\mathbf{r}'} J_{\mathbf{r},\mathbf{r}'} m_{\mathbf{r}} m_{\mathbf{r}'} - T \sum_{\mathbf{r}} \ln \left[2 \cosh \left(\frac{h_{\mathbf{r}}}{T} \right) \right], \quad (3)$$

where here and in the following we set $k_B = 1$. The mean-field acting on site $\mathbf{r}$ is given by

$$h_{\mathbf{r}} = \sum_{\mathbf{r}'} J_{\mathbf{r},\mathbf{r}'} m_{\mathbf{r}'}. \quad (4)$$

Minimising the free energy with respect to the local magnetisations gives rise to the coupled self-consistency equa-

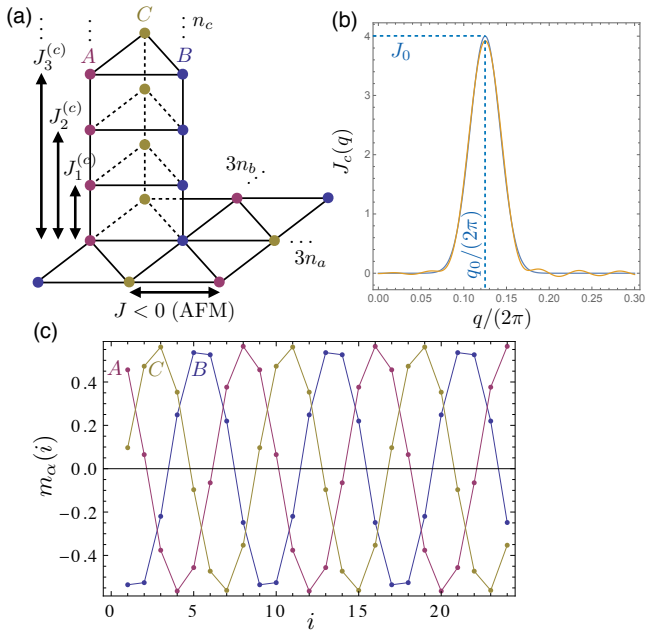

FIG. 18. (a) Exchange couplings of the effective three-dimensional Ising model and resulting three sub-lattice structure. (b) The exchange couplings $J_i^{(c)}$ between i-th neighbours along the chain direction c are parametrised in momentum space, $J_c(q) = J_0 \exp[-(|q| - q_0)^2/b^2]$. The blue curve shows $J_c(q)$ for $J_0 = 4.0$, $\delta = q_0/(2\pi) = 1/8$ and $b = 0.05\pi$. The orange curve shows the approximate $J_c(q)$ obtained retaining the only first ten nearest neighbour couplings along **c**. (c) Shows the magnetisation obtained in the mean field calculation for sites $\alpha = A, B, C$ as a function of cite index i along the c-axis

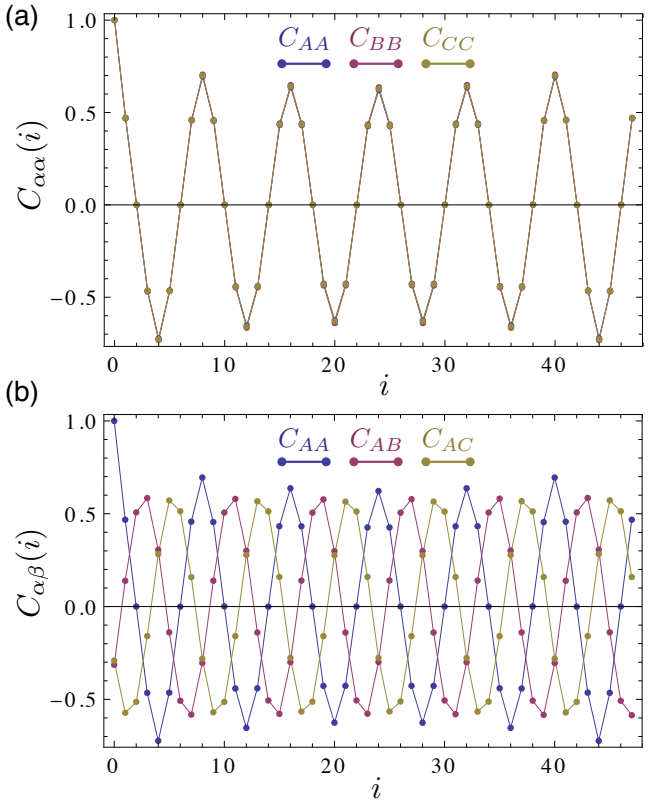

FIG. 19. Spin-spin correlation functions along the chains (a) and between neighbouring chains (b), calculated from Monte-Carlo sampling. Here i denotes the separation of the spins along the chain direction (c-axis).

tions

$$m_{\mathbf{r}} = \tanh\left(\frac{h_{\mathbf{r}}}{T}\right). \tag{5}$$

SI Fig. 18c shows the solution of the self-consistent mean-field equations for a system of $3 \times 3 \times 24$ lattice sites with Ising spins and exchange couplings $J_0 = 4.0$, $J = -0.5$ and $T < T_N$. As expected, the system develops SDW order with a period of 8 lattice spacings along the c-axis. While the SDWs on the three sub-lattices have the same amplitudes, their phases are shifted by $\Delta\phi = 2\pi/3$. These findings are robust over a wide range of temperatures and exchange couplings, provided that the coupling J between the chains is antiferromagnetic and sufficiently small.

It is possible to obtain an analytic understanding of these findings by expanding the mean-field free energy (3) near T_N. In this regime $h_{\mathbf{r}}/T \ll 1$, and the free energy per triangle is

$$f_{\rm MF} = \frac{1}{2}\sum_\alpha \int_q (J_c(q) - 3J)\left(1 - \frac{J_c(q) - 3J}{T}\right)|m_\alpha(q)|^2$$

$$+\frac{3J}{2}\int_q \left(1 - \frac{3J + 2J_c(q)}{T}\right)|M(q)|^2 + \mathcal{O}(m^4), \tag{6}$$

where q is the momentum along **c**, $\alpha = A, B, C$ denotes the sub-lattice, and

$$M(q) = \sum_\alpha m_\alpha(q), \tag{7}$$

where $m_\alpha(q) = |m_\alpha(q)|e^{i\phi_\alpha}$.

From the first line of Eq. (6) it follows that the chains order with a modulation vector corresponding to the maximum of $J_c(q)$. The ordering transition temperature is given by

$$T_N = J_0 - 3J. \tag{8}$$

The above argument neglects the second line of Eq. (6), which contains a coupling between the chains. At $T = T_N$, the coefficient of $|M(q)|^2$ is positive for $0 < -J < J_0/6$. For weakly coupled chains, the transition is therefore into a state with $M(2\pi\delta) = 0$. Since slightly below T_N the amplitudes of the three SDWs are equal, the phases of the SDWs must satisfy

$$\sum_{\alpha} e^{i\phi_\alpha} = 0, \tag{9}$$

which implies a relative phase of $2\pi/3$ between neighbouring chains.

Monte-Carlo Study

Fluctuations can play an important role in systems with geometric frustration. An example is the Heisenberg antiferromagnet on the triangular lattice. In this model, quantum fluctuations can drive a transition from the classical 120 degree ground state to a collinear state. For the three dimensional Ising model for UAu_2, the mean-field level analysis shows that the geometric frustration in the triangular lattice planes gives rise to 120 degree phase shifts between the SDWs on neighbouring chains. This state could be unstable against thermal fluctuations beyond mean-field. To investigate this possibility we performed Monte-Carlo simulations of systems of $9 \times 9 \times 48$ lattice sites with periodic boundary conditions, using the same exchange parameters as in the mean-field analysis.

We sampled configurations $\{\sigma_{\mathbf{r}}\}$ ($\sigma_{\mathbf{r}} := \hat{S}^z_{\mathbf{r}} = \pm 1$) from the probability distribution

$$p\left(\{\sigma_{\mathbf{r}}\}\right) = \frac{e^{-\beta E(\{\sigma_{\mathbf{r}}\})}}{\sum_{\{\sigma_{\mathbf{r}}\}} e^{-\beta E(\{\sigma_{\mathbf{r}}\})}}, \tag{10}$$

using Metropolis sampling with single-site, spin-flip updates. Here, $\beta = 1/T$ denotes the inverse temperature and $E\left(\{\sigma_{\mathbf{r}}\}\right)$ is the energy of the configuration. We find that fluctuations lead to a slight reduction of the ordering temperature of about 5-10 %. As expected, the ordered state is characterised by a three sub-lattice structure. To analyse the magnetic structure we calculated the correlation functions

$$C_{\alpha\beta}(i) = \frac{1}{n_c} \sum_{j} \langle \sigma_\alpha(j) \sigma_\beta(j+i) \rangle \,, \tag{11}$$

by averaging over the sampled configurations at a given temperature. Here, $C_{\alpha\alpha}(i)$ denotes the spin-spin correlation function along the chains on sub-lattice α, as a function of the distance i between the spins. $C_{\alpha\beta}(i)$ with $\alpha \neq \beta$ are the correlation functions between neighbouring chains.

SI Fig. 19a shows that the correlation functions along the chains are the same on the three sub-lattices, demonstrating that the SDWs have the same amplitudes. The intra-chain correlations $C_{\alpha\alpha}$ are not sensitive to the phases ϕ_α of the SDWs, however. SI Fig. 19b shows that $C_{AB}(i)$ and $C_{AC}(i)$ are shifted by phases $2\pi/3$ and $4\pi/3$ with respect to $C_{AA}(i)$. This demonstrates that the relative phase between SDWs on the different sub lattices is $2\pi/3$.

It is also possible to understand why $C_{AB}(0) = C_{AC}(0) \approx -1/3$. Below T_N, the averages are dominated by configurations for which there is one frustrated bond on each triangle. If for example $\sigma_A = +1$, then we expect $(\sigma_B, \sigma_C) = (+1, -1), (-1, +1)$ or $(-1, -1)$ implying that $\langle \sigma_A \sigma_B \rangle = \langle \sigma_A \sigma_C \rangle = -1/3$.

To summarise, both unrestricted mean-field calculations and Monte-Carlo simulations show that the three dimensional Ising model with RKKY interactions that are peaked at the ordering vector $(1/3, 1/3, \delta)$ not only give rise to the correct Bragg peaks but also explain that the SDWs on the three sub-lattices have the same amplitudes and relative phase shifts of $2\pi/3$.

CALCULATION OF THE HEAT CAPACITY

The two channel Kondo model

The Anderson impurity model that describes the valence fluctuations between U^{3+} and U^{4+}, with ground state and excited state doublets is given by [69, 70]

$$\begin{aligned}
\hat{\mathcal{H}} &= \hat{\mathcal{H}}_0 + \hat{\mathcal{H}}_\eta, \\
\hat{\mathcal{H}}_0 &= \sum_{\mathbf{k}\tau\sigma} \left(\epsilon_{\mathbf{k}} - \frac{1}{2}\sigma h \right) c^\dagger_{\mathbf{k}\tau\sigma} c_{\mathbf{k}\tau\sigma} + \epsilon_2 \sum_{\tau=\pm 1} g^\dagger_\tau g_\tau \\
&\quad + \epsilon_3 \sum_{\sigma=\uparrow,\downarrow} f^\dagger_\sigma f_\sigma - \frac{1}{2} h \left(f^\dagger_\uparrow f_\uparrow - f^\dagger_\downarrow f_\downarrow \right), \\
\hat{\mathcal{H}}_\eta &= \eta \sum_{\mathbf{k}\tau\sigma} \left(c^\dagger_{\mathbf{k}\tau\sigma} g^\dagger_{-\tau} f_\sigma + f^\dagger_\sigma g_{-\tau} c_{\mathbf{k}\tau\sigma} \right),
\end{aligned} \tag{12}$$

subject to the constraint

$$1 = \sum_{\tau=\pm 1} g^\dagger_\tau g_\tau + \sum_{\sigma=\uparrow,\downarrow} f^\dagger_\sigma f_\sigma = \hat{n}_g + \hat{n}_f. \tag{13}$$

Here, ϵ_2 and ϵ_3 denote the energies of the ground doublets in the $5f^2$ (U^{4+}) and $5f^3$ (U^{3+}) configurations, respectively. g_τ are Fermion annihilation operators for localised U^{4+} states of pseudospin τ and f_σ Fermion annihilation operators for localised U^{3+} states of spin σ. Note that the conduction electron operators $c_{\mathbf{k}\tau\sigma}$ are expanded in the angular momentum channels of the impurity and hence carry both quantum numbers σ and τ. An applied magnetic field h breaks the spin degeneracy of the conduction bands and splits the U^{3+} Kramers doublet. If the quadrupole ($5f^2$ doublet) also has a dipole moment it will also be split (by field along the c-axis), not shown in the above. For clarity we will refer to this degree of freedom as pseudopspin and associated the moments as simply a quadrupole moment in the following.

The first term in $\hat{\mathcal{H}}_\eta$ that describes valence fluctuations corresponds to a $5f^3$ (U^{3+}) to $5f^2$ (U^{4+}) transition, transferring an electron to the conduction sea. This process conserves the total angular momentum and charge. The second term is the reverse process.

In the absence of valence fluctuations, $\eta = 0$, the U^{4+} quadrupole doublet is the groundstate if the energy $\Delta E = \epsilon_3 - (\epsilon_2 + \epsilon_F) = \Delta - \epsilon_F$ is positive. The corresponding Kondo impurity model is obtained from a canonical transformation, $\hat{\mathcal{H}}' = e^{\hat{S}}\hat{\mathcal{H}}e^{-\hat{S}}$, where to leading order, $\hat{S}$ is determined such that the linear valence-fluctuation term is transformed away. This leads to $\hat{\mathcal{H}}' = \hat{\mathcal{H}}_0 + \delta\hat{\mathcal{H}}'$ with $\delta\hat{\mathcal{H}}' \approx \hat{\mathcal{H}}_\eta (E_0 - \hat{\mathcal{H}}_0)^{-1} \hat{\mathcal{H}}_\eta$.

For $\eta \ll |\Delta E|$ this reduces to a two-channel Kondo model [69, 70] with an integer valence. For a pure U^{4+} ground state ($\langle \hat{n}_f \rangle = 0$ and $\langle \hat{n}_g \rangle = 1$) we obtain the Kondo impurity Hamiltonian

$$\delta\hat{\mathcal{H}}' = \frac{J_K}{2} \sum_{\mathbf{k},\mathbf{k}'} \sum_{i=x,y,z} \hat{T}^i \Psi^\dagger_{\mathbf{k}'} \left(\boldsymbol{\tau}^i \otimes \mathbf{1}\right) \Psi_{\mathbf{k}} + \zeta \frac{J_K}{2} \sum_{\mathbf{k},\mathbf{k}'} \sum_{i=x,y,z} \hat{T}^i \Psi^\dagger_{\mathbf{k}'} \left(\boldsymbol{\tau}^i \otimes \boldsymbol{\sigma}^z\right) \Psi_{\mathbf{k}}, \quad (14)$$

where we have combined the Fermion operators $c_{\mathbf{k}\tau\sigma}$ with spin and pseudo-spin flavours into a four-component spinor $\Psi_{\mathbf{k}}$. The first line describes the Kondo coupling between the local quadrupole impurity $\hat{\mathbf{T}}$ and the conduction electron pseudo-spin operator. $\boldsymbol{\tau}^i$ and $\boldsymbol{\sigma}^z$ denote Pauli matrices in pseudo-spin space and spin space. The electron spin $\sigma = \uparrow, \downarrow$ provides the two channels of the Kondo problem. The Kondo coupling is equal to

$$J_K = \frac{\eta^2}{\Delta E - h} + \frac{\eta^2}{\Delta E + h}. \quad (15)$$

A field h splits the Kramers doublet giving rise to an anisotropy between the channels, given by the second line in Eq. (14), with

$$\zeta = \frac{h}{\Delta E}, \quad (16)$$

valid for $|\zeta| \ll 1$. $\hat{H}_0$ also includes a term that describes splitting of the conduction band in a field $\sum_{\mathbf{k}} h \Psi^\dagger_{\mathbf{k}} (\mathbf{1} \otimes \boldsymbol{\sigma}^z) \Psi_{\mathbf{k}}$, and a similar term for the dipole moments associated with the quadrupole index. From here on we use ζ to account for all sources of channel splitting. The values of the coupling for spin up and spin down channels are $J_1 = J_K(1+\zeta)$ and $J_2 = J_K(1-\zeta)$. For theoretical convenience, the coupling (J_K and ζJ_K) are considered to be anisotropic having the values J_{Kz} and $\zeta_z J_{Kz}$ for pseudospin direction $i = z$ and $J_{K\perp}$ and $\zeta_\perp J_{K\perp}$ for $i = x, y$.

The differences in scattering phase shift between pseudospin parallel and antiparallel to the z-axis, evaluated for the two spin channels $n = 1, 2$ are $\delta_n = 2\tan^{-1}(\pi J_{nz}\nu_0/4)$. Here, $\nu_0 = 1/(2\pi v_f)$ is the one dimensional energy density of states per spin per channel per sample radius for scattering at the Fermi level [71] (v_f is the Fermi velocity). There is a well known exact solution of the two channel Kondo model, namely Hamiltonian $\mathcal{H}'$ (defined above EQN 14), for $\zeta = 0$ and a specific values $\delta_1 = \delta_2 = \pi/2$ that define the locus of the Emery-Kivelson (EK) fixed line [72, 73]. In EQN 14, the conduction electron field Ψ has 4 components. These map to two interacting spinless scalar fields ψ and ψ_s and two non-interacting fields (which are dropped) [71]. The field ψ_s corresponds to fluctuations of the quadrupole moment and ψ to combined fluctuations of both spin and quadrupole in our case. The components of the impurity operator can be rewritten in terms of a spinless Fermion operator $\hat{d}$ as $\hat{T}^z = \hat{d}^\dagger\hat{d} - \frac{1}{2}$, $\hat{T}^+ = \hat{T}_x + i\hat{T}_y = \hat{d}^\dagger$ and $\hat{T}^- = \hat{T}_x - i\hat{T}_y = \hat{d}$. These spinless Fermions can be further decomposed into two Majorana Fermions $\hat{a} = i(\hat{d} - \hat{d}^\dagger)$ and $\hat{b} = (\hat{d} + \hat{d}^\dagger)$ (so that $\hat{T}_z = i\hat{a}\hat{b}$, $\hat{T}_x = \hat{b}/2$, $\hat{T}_y = \hat{a}/2$). The final equivalent Hamiltonian is [71]

$$H = H_0(\psi, \psi^\dagger) + H_0(\psi_s, \psi_s^\dagger) - \bar{\lambda} i \left[\psi(0) + \psi^\dagger(0)\right] \hat{a} + \delta\lambda \left[\psi^\dagger(0) - \psi(0)\right] \hat{b} + \left[W\psi^\dagger(0)\psi(0) + V\psi_s^\dagger(0)\psi_s(0) + Z\right] i\hat{a}\hat{b}. \quad (17)$$

The direct coupling of the conduction electrons to the magnetic field is contained in the free Fermion H_0 terms. The values of the coefficients [71] are

$$\bar{\lambda} = \frac{1}{2} \sum_{n=1,2} \frac{J_{n\perp}\sqrt{\nu_0 \xi}}{2} \frac{\cos^2(\delta_n/2)}{\sin(\bar{\delta})} \quad (18)$$

$$\delta\lambda = \frac{1}{2} \sum_{n=1,2} (-1)^n \frac{J_{n\perp}\sqrt{\nu_0 \xi}}{2} \frac{\cos^2(\delta_n/2)}{\sin(\bar{\delta})} \quad (19)$$

$$W = \frac{2}{\pi\nu_0} \tan\left(\frac{\delta_1 - \delta_2}{2}\right) \quad (20)$$

$$V = \frac{2}{\pi\nu_0} \cot(\bar{\delta}) \quad (21)$$

with $\bar{\delta} = (\delta_1 + \delta_2)/2$. V measures how far the system is from the EK line and is zero on the line. Z is proportional to the splitting of the ground state doublet, present if it has a dipole moment. In the following we set $Z = 0$ for simplicity as it does not affect our conclusions. Both W and $\delta\lambda$ are proportional to the channel splitting ζ. The zero field expression is quadratic in the Fermion operators when $V = W = 0$ and is therefore exactly solvable as previously stated. ξ is an energy cut-off (e.g. from the bandwidth). The heat capacity on the Emery-Kivelson fixed line, which we denote C_{EK}, does not diverge as $T \to 0$ and has no logarithmic term. The corrections due to finite $\zeta_\perp$ (i.e. $J_{1\perp} \neq J_{2\perp}$) can be included in this analysis. The resulting expression for C/T is [71]

$$\frac{C_{\rm EK}}{T} = \frac{R\,\Gamma}{2\pi T^2} \left[1 - \frac{\Gamma}{2\pi T} \psi^{(1)}\left(\frac{1}{2} + \frac{\Gamma}{2\pi T}\right)\right] + \frac{R\,\Gamma\zeta_\perp^2}{2\pi T^2} \left[1 - \frac{\Gamma\zeta_\perp^2}{2\pi T} \psi^{(1)}\left(\frac{1}{2} + \frac{\Gamma\zeta_\perp^2}{2\pi T}\right)\right] \quad (22)$$

where $\psi^{(1)}$ is the first derivative of the Digamma function with $\Gamma = 4\pi\nu_0\bar{\lambda}^2 \approx \frac{4}{\pi}\xi$ (the last approximation is for $J_\perp = J_z$ and $\zeta_\parallel, \zeta_\perp \ll 1$) and $\zeta_\perp = \delta\lambda/\bar{\lambda}$. This formula captures the release of the residual entropy

$0.5R\log(2)$ with splitting, $\zeta_\perp$. Most of the entropy is released uniformly with temperature over the temperature scale $T_s = \Gamma\zeta_\perp^2$. In zero field, $C_{\rm EK}/T$ approaches a constant $C/T \sim 0.52R/\Gamma$ (with Γ in Kelvin) below $T \lesssim 0.1\Gamma$ and falls off in the range $0.1\Gamma \lesssim T \lesssim \Gamma$ only very approximately logarithmically crossing over to a high temperature dependence $C/T \sim R\Gamma/(2\pi T^2)$. The high temperature entropy in this model is $R\log(2)$ and does not include any contribution from occupying the excited doublet, projected out in the early part of the derivation.

The correction to the heat capacity for J_z different from the EK value (i.e. $0 < V \ll 1$) can be calculated [73] with second order perturbation theory, which for $\zeta_z = 0$ (i.e. no splitting of J_z and δ) gives a contribution to the heat capacity,

$$\frac{\Delta C}{T} = -\frac{\partial}{\partial T^2}\frac{V^2}{2}\left\{\int_0^{1/T} d\tau\ G_s^2(\tau)A(\tau)B(\tau) - G_s(0)^2\int_0^{1/T} d\tau A(\tau)B(\tau)\right\} \quad (23)$$

with $A(\tau) = -\langle Ta(\tau)a(0)\rangle$, $B(\tau) = -\langle Tb(\tau)b(0)\rangle$ and $G(\tau) = -\langle T\psi_s(0,\tau)\psi_s^\dagger(0,0)\rangle$. These terms are explicitly,

$$\begin{aligned} A(\tau) &= \frac{1}{\beta}\sum_{\omega_n=\frac{(2n+1)}{\beta}} \frac{e^{i\omega_n\tau}}{i\omega_n + i\Gamma\ {\rm sgn}(\omega_n)} \\ &= \frac{\beta\Gamma}{\pi}\int_{-\infty}^{\infty} dx \frac{1}{e^x+1}\frac{e^{\frac{\tau}{\beta}x}}{x^2+(\beta\Gamma)^2}, \quad (24) \\ G_s(\tau) &= \frac{1}{\beta}\sum_{\omega_n}\int_{-\xi/v_f}^{\xi/v_f}\frac{dk}{2\pi}\frac{e^{i\omega_n\tau}}{i\omega_n - v_f k + g_s h} \\ &= \frac{1}{2\pi\beta v_f}\int_{\beta(-\xi-g_s h)}^{\beta(\xi-g_s h)} dx \frac{e^{\frac{\tau}{\beta}x}}{e^x+1}, \quad (25) \\ G_s(0) &\underset{\xi\to\infty}{=} -G_s(\beta) = \frac{g_s h}{2\pi}. \quad (26) \end{aligned}$$

$B(\tau)$ is given by the same expression as $A(\tau)$ but with $\Gamma \to \Gamma\zeta_\perp^2$. $g_s h$ is the splitting of the opposite quadrupole conduction electron bands. The linear in h corrections to G_s are antisymmetric about $\tau = \beta/2$ and do not result in a linear in h contribution to C/T.

The first integral in EQN 23 is responsible for the $\log(T)$ heat capacity of the 2 channel Kondo effect in zero magnetic field [73] noting that $B = 1/2$ when $\zeta_\perp = 0$. For $T \ll \Gamma$, $\Delta C/T \sim a\log(T^*/T)$ with $a \sim (2/\pi)(R/\Gamma)\cot(\bar{\delta})^2$ (independent of the energy cutoff ξ) and $T^* \sim 0.085\Gamma$ (calculated numerically for $\xi \sim (\pi/4)\Gamma$). $\int_0^\infty \Delta C/T = 0$, since the total entropy is already counted in the EK part. A finite channel asymmetry reduces $B < 1/2$, and suppresses this contribution to C/T at low temperature. There are additional contributions, for example from the W term that are proportional to $\zeta_\perp^2$. C/T in field is however dominated by the entropy release in the $C_{\rm EK}/T$ term.

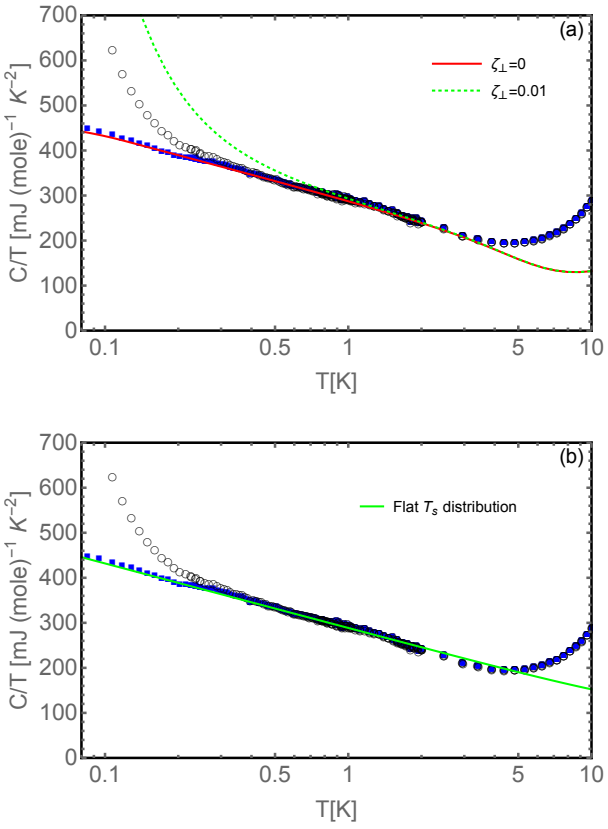

FIG. 20. Heat capacity divided by temperature. The open circles are measured values. Below ~ 1 K these are in a field of 1.5 T ($B \parallel c$) to avoid a zero field bump below 500 mK (see text) and have been extended to higher temperature with zero field data. The solid points show the same data after subtracting a $1/T^3$ term attributed to a Schottky tail from nuclear quadrupole moments. The upturn in the experimental heat capacity above 4 K is due to phonons. In (a) the solid red line is the calculated dependence for the two channel Kondo model for the parameters described in the text. The dashed line (green) is the calculation for a channel splitting $\zeta_\perp = 0.01$ that corresponds to an applied field of order 1.5 T. The field induced release of entropy contrasts with the experimental data, showing that 2CK physics for a single site cannot explain the observed C/T. In (b) the solid green line is the calculated dependence for a uniform distribution of T_s which characterises the channel asymmetry (the calculation parameters are given in the text).

$C = \gamma T + C_{\rm EK}(T) + \Delta C(T)$ (with γ a Sommerfeld contribution from the conduction electrons) from EQNs 22 and 23, for one Kondo site per formula can be compared with the experimental data. The calculation is compared with the data at 1.5 T in Fig. 20a, with a nuclear Schottky ($1/T^3$) term subtracted. We first consider the theoretical result for $H = 0$ and then include the effect of the field. The parameters $\Gamma = 50K$, $\delta = 0.6(\pi/2)$ and $\gamma = 110$mJ mole$^{-1}K^{-2}$ used for the calculation are not determined uniquely by the low temperature experimen-

tal data; different values of Γ can be chosen. $\Gamma > 16$K is required to have $\gamma > 0$. The required value for $\cot(\delta)$ increases with Γ with a broad maximum for the corresponding value of $\gamma \approx 115$ mJ mole$^{-1}K^{-2}$ that is only slightly below γ in the F-state. The value of $\Gamma = 50$ K has been chosen to reproduce the slight down turn in C/T at higher temperature.

The application of a magnetic field of 1.5 T corresponds to $\zeta_\perp = h/\Delta E \approx 0.01$, based on $\Delta E = 50$ K and a moment of 1 μ_B in EQNS 15 and 16. The calculated heat capacity for $\zeta_\perp = 0.01$ is also shown in Fig. 20a. Even though $\Gamma\zeta_\perp^2$ is much lower than the lowest temperature accessible in the experiment, there is a clear change in the calculated curve with field that is not seen experimentally, which comes from the high temperature tail of the entropy release which has the form $C/T \sim \Gamma\zeta_\perp^2/(2\pi T^2)$ for $T \gg \Gamma\zeta_\perp^2$.

In the next section we explore whether a distribution of larger values of $T_s = \Gamma\zeta_\perp^2$ can instead account for $C/T \sim \log(T)$.

The heat capacity for a distribution of T_s

As described above most of the entropy $0.5R\log(2)$ is released uniformly with temperature between zero temperature and $T_s = \Gamma\zeta_\perp^2$. A heat capacity $C/T \sim \log(1/T)$ in the temperature range $T_{\rm min} < T < T_{\rm max}$ is obtained for a flat distribution of T_s over the range $T_{\rm min}$ to 10 $T_{\rm max}$. In Fig. 20b, the experimental data is plotted alongside the calculated dependence for a flat distribution of T_s between 0 and 70 K (from the second term in EQN 22) plus a Sommerfeld term $\gamma = 90$ mJK^{-2}mole^{-1} (which includes the contribution from the first term in EQN 22 with $\Gamma \gg T$).

[1] A.J. Schofield, Contemporary Physics **40**, 95 (1999).
[2] P. Coleman, C. Pépin, Q. Si, and R. Ramazashvili, Journal of Physics: Condensed Matter **13**, R723 (2001).
[3] B.Keimer, S.A. Kivelson, M.R. Norman, S. Uchida, and J. Zaanen, Nature **518**, 179 (2015).
[4] B. Michon and et al., Nature **567**, 218 (2019).
[5] S.D. Chen and et al., Science **366**, 1099 (2019).
[6] P. Gegenwart, Q. Si, and F. Steglich, Nature Physics **4**, 186 (2008).
[7] M. Vojta, Reports on Progress in Physics **81**, 064501 (2018).
[8] C. Pfleiderer and et al., Nature **414**, 427 (2001).
[9] N. Doiron-Leyraud and et al., Nature **425**, 595 (2003).
[10] C. Pfleiderer and et al., Nature **427**, 227 (2004).
[11] R. Ritz and et al., Nature **497**, 231 (2013).
[12] Y. Masumoto and et al., Science **331**, 316 (2011).
[13] T. Tomita, K. Kuga, Y. Uwatoko, and S. Nakatsuji, Journal of Physics: Conference Series **592**, 012019 (2015).
[14] R.M. Potok, I.G. Rau, H. Shtrikman, Y. Oreg, and D. Goldhaber-Gordon, Nature **446**, 167 (2007).
[15] T. Onimaru and H. Kusunose, Journal of the Physical Society of Japan **85**, 082002 (2016).
[16] Y. Yamane and et al., Phys. Rev. Lett. **121**, 077206 (2018).
[17] C.L. Seaman and et al., Phys. Rev. Lett. **67**, 2882 (1991).
[18] I. Affleck and A.W.W. Ludwig, Phys. Rev. B **48**, 7297 (1993).
[19] E. Miranda and V. Dobrosavljević, Reports on Progress in Physics **68**, 2337 (2005).
[20] C. Pfleiderer and et al., Science **316**, 1871 (2007).
[21] A. Miyake and et al., Journal of the Physical Society of Japan **78**, 044703 (2009).
[22] M. Kontani and et al., Journal of the Physical Society of Japan **63**, 3421 (1994).
[23] R. Pöttgen, V.H. Tran, R.D. Hoffmann, D. Kaczorowski, and R. Troc, J. Mater. Chem. **6**, 429 (1996).
[24] O. A. Starykh, Reports on Progress in Physics **78**, 052502 (2015).
[25] Q. Sheng and C. L. Henley, Journal of Physics: Condensed Matter **4**, 2937 (1992).
[26] M. Kuburagi, T. Tonegawa, and J. Kanamori, Journal of the Physical Society of Japan **51**, 3857 (1982).
[27] N. Todoroki and S. Miyashita, Journal of the Physical Society of Japan **73**, 412 (2004).
[28] O.Koseki and F. Matsubara, Journal of the Physical Society of Japan **69**, 1202 (2000).
[29] J. Villain, R. Bidaux, J.P. Carton, and R. Conte, J. Phys. France **41**, 1263 (1980).
[30] D. Gignoux and D. Schmitt, *Handbook of Magnetic Materials*, Chap. 2: Magnetism of compounds of rare earths with non-magnetic metals, Vol. 10 (Elsevier Science B.V, North-Holland, 1997) pp. 239–413.
[31] S. Agrestini, C. Mazzoli, A. Bombardi, and M.R. Lees, Phys. Rev. B **77**, 140403 (2008).
[32] S. Agrestini, C.L. Fleck, L.C. Chapon, C. Mazzoli, A. Bombardi, M.R. Lees, and O.A. Petrenko, Phys. Rev. Lett. **106**, 197204 (2011).
[33] J.P Hill, G. Helgesen, and D. Gibbs, Phys. Rev. B **51**, 10336 (1995).
[34] V.J. Emery, S.A. Kivelson, and J.M. Tranquada, Proceedings of the National Academy of Sciences **96**, 8814 (1999).
[35] U. Walter, Journal of Physics and Chemistry of Solids **45**, 401 (1984).
[36] A.J. Millis, Phys. Rev. B **48**, 7183 (1993).
[37] H. v. Löhneysen, A. Rosch, M. Vojta, and P. Wölfle, Rev. Mod. Phys. **79**, 1015 (2007).
[38] J.R. Schrieffer, Journal of Low Temperature Physics **99**, 397 (1995).
[39] J. Custers and et al., Nature Materials **11**, 189 (2012).
[40] V. Martelli and et al., Proceedings of the National Academy of Sciences **116**, 17701 (2019).
[41] Q. Si, Physica B: Condensed Matter **378-380**, 23 (2006).
[42] S. Doniach, Physica B+C **91**, 231 (1977).
[43] M. Dzero, M.R. Norman, I. Paul, C. Pépin, and J. Schmalian, Phys. Rev. Lett. **97**, 185701 (2006).
[44] D. L. Cox and A. Zawadowski, Advances in Physics **47**, 599 (1998).
[45] P.D. Sacramento and P. Schlottmann, Phys. Rev. B **43**, 13294 (1991).

[46] Y.Shimizu, O. Sakai, and S. Suzuki, Journal of the Physical Society of Japan **67**, 2395 (1998).

[47] M.Fabrizio, A.O. Gogolin., and P. Nozières, Phys. Rev. Lett. **74**, 4503 (1995).

[48] H. Amitsuka, K. Kuwahara, M. Yokoyama, K. Tenya, T. Sakakibara, M. Mihalik, and A.A. Menovský, Physica B: Condensed Matter **281-282**, 326 (2000).

[49] E. Miranda, V. Dobrosavljevic, and G. Kotliar, Journal of Physics: Condensed Matter **8**, 9871 (1996).

[50] A.I. Tóth and G. Kotliar, Phys. Rev. Lett. **107**, 266405 (2011).

[51] S. Nishiyama, H. Matsuura, and K. Miyake, Journal of the Physical Society of Japan **79**, 104711 (2010).

[52] S. Nishiyama and K. Miyake, Journal of the Physical Society of Japan **80**, 124706 (2011).

[53] C.J. Bolech and N. Andrei, Phys. Rev. B **71**, 205104 (2005).

[54] G.G. Blesio, L.O. Manuel, A.A. Aligia, and P. Roura-Bas, Phys. Rev. B **100**, 075434 (2019).

[55] L. C. Chapon and et al., Neutron News **22**, 22 (2011).

[56] The Elk FP-LAPW code, http://elk.sourceforge.net (2017).

[57] J.P. Perdew, K. Burke, and M. Ernzerhof, Phys. Rev. Lett. **77**, 3865 (1996).

[58] A.I. Liechtenstein, V.I. Anisimov, and J. Zaanen, Phys. Rev. B **52**, R5467 (1995).

[59] M.R. Norman, Phys. Rev. B **52**, 1421 (1995).

[60] F. Bultmark, F. Cricchio, O. Grånäs, and L. Nordström, Phys. Rev. B **80**, 035121 (2009).

[61] M.A. Ruderman and C. Kittel, Phys. Rev. **96**, 99 (1954).

[62] P. Raghavan, Atomic Data and Nuclear Data Tables **42**, 189 (1989).

[63] A.C. Jacko, J.O. Fjærestad, and B.J. Powell, Nature Physics **5**, 422 (2009).

[64] J. Rodríguez-Carvajal, Physica B: Condensed Matter **192**, 55 (1993).

[65] A.S. Wills, Physica B: Condensed Matter **276-278**, 680 (2000).

[66] P.J. Brown, *International Tables for Crystallography Volume C: Mathematical, physical and chemical tables* (John Wiley & Sons Ltd, 2006) pp. 454–461.

[67] G. van der Laan and B.T. Thole, Phys. Rev. B **53**, 14458 (1996).

[68] J. L. Schmehr, *PhD thesis*, Ph.D. thesis, University of Edinburgh (2015).

[69] D.L. Cox, Phys. Rev. Lett. **59**, 1240 (1987).

[70] A. Schiller, F.B. Anders, and D.L. Cox, Phys. Rev. Lett. **81**, 3235 (1998).

[71] M. Fabrizio, A.O. Gogolin, and P. Nozières, Phys. Rev. B **51**, 16088 (1995).

[72] V.J. Emery and S. Kivelson, Phys. Rev. B **46**, 10812 (1992).

[73] A.M. Sengupta and A. Georges, Phys. Rev. B **49**, 10020 (1994).